

Field-free switching of perpendicular magnetization through spin-orbit torque in antiferromagnet/ferromagnet/oxide structures

Young-Wan Oh^{1,*}, Seung-heon Chris Baek^{1,2,*}, Y. M. Kim¹, Hae Yeon Lee¹, Kyeong-Dong Lee¹, Chang-Geun Yang^{3,4}, Eun-Sang Park^{4,5}, Ki-Seung Lee³, Kyoung-Whan Kim^{6,7,8,9}, Gyungchoon Go³, Jong-Ryul Jeong¹⁰, Byoung-Chul Min⁴, Hyun-Woo Lee⁶, Kyung-Jin Lee^{3,5,**} and Byong-Guk Park^{1,**}

¹*Department of Materials Science and Engineering and KI for Nanocentury, KAIST, Daejeon 34141, Korea*

²*School of Electrical Engineering, KAIST, Daejeon 34141, Korea*

³*Department of Materials Science and Engineering, Korea University, Seoul 02841, Korea*

⁴*Center for Spintronics, Korea Institute of Science and Technology, Seoul 02792, Korea*

⁵*KU-KIST Graduate School of Converging Science and Technology, Korea University, Seoul 02841, Korea*

⁶*PCTP and Department of Physics, Pohang University of Science and Technology, Pohang 37673, Korea*

⁷*Center for Nanoscale Science and Technology, National Institute of Standards and Technology, Gaithersburg, Maryland 20899, USA*

⁸*Maryland Nanocenter, University of Maryland, College Park, MD 20742, USA*

⁹*Basic Science Research Institute, Pohang University of Science and Technology, Pohang 37673, Korea*

¹⁰*Department of Materials Science and Engineering, Graduate School of Energy Science Technology, Chungnam National University, Daejeon 34134, Korea*

*These authors equally contributed to this work.

**Corresponding emails: kj_lee@korea.ac.kr (K.-J.L.) and bgpark@kaist.ac.kr (B.-G.P.).

Spin-orbit torques arising from the spin-orbit coupling of non-magnetic heavy metals allow electrical switching of perpendicular magnetization. The switching is however not purely electrical in laterally homogeneous structures, since for deterministic switching, an additional in-plane magnetic field is required, which is detrimental for device applications. On the other hand, if antiferromagnets can generate spin-orbit torques, they may enable all-electrical deterministic switching since the desired magnetic field may be replaced by their exchange bias. Here we report sizable spin-orbit torques in IrMn/CoFeB/MgO structures. The antiferromagnetic IrMn layer also supplies an in-plane exchange-bias field, which enables all-electrical deterministic switching of perpendicular magnetization without any assistance from an external magnetic field. Together with sizable spin-orbit torques, these features make antiferromagnets a promising candidate for future spintronic devices. We also show that the signs of spin-orbit torques in various IrMn-based structures go beyond existing theories, which demand significant theoretical progress.

The principal discipline of spintronics is the robust generation, control, and detection of spin currents in various classes of materials¹. An emerging branch of spintronics pursues the use of antiferromagnets² where the magnetic moments are compensated on an atomic scale to make the total magnetization vanish and to suppress stray field³, which is a primary source of hazardous magnetic perturbations in integrated devices. Together with the high operating frequency of antiferromagnets in the terahertz ranges⁴, which allow ultrafast information processing superior to gigahertz-range operating frequency of ferromagnets, these features make antiferromagnets attractive materials for next generation spintronics. On the other hand, building a viable spintronic device based on antiferromagnets requires the ability to induce

experimentally observable effects across the zero total magnetization in the material as well as the technology to control the antiferromagnetic order against the strong magnetocrystalline anisotropy in antiferromagnets. Owing to these challenges, research toward this direction has been limited for a long time to using antiferromagnets only as exchange biasing tools for ferromagnets⁵. Some progress has been achieved recently, which shows the spin-transfer torque effects in antiferromagnets⁶⁻⁸ and the possibility of utilizing antiferromagnets as one of the electrodes in magnetic tunnel junctions^{9,10} and antiferromagnet memories³, taking the advantage of zero stray fields to minimize the magnetic perturbations between neighboring devices.

Moreover, recent reports of interesting spin-orbit coupling effects in antiferromagnets¹¹⁻¹³ imply possibility to elevate antiferromagnets from passive to active device elements that generate spin current themselves to become an alternative to heavy metals in heavy metal/ferromagnet/oxide structures for spin-orbit-torque-active devices. Experiments with heavy-metal-based structures demonstrate that spin-orbit torques enable efficient current-induced switching of perpendicular magnetization^{14,15} and domain wall motion with high speed^{16,17}. By replacing heavy metals with antiferromagnets, two important benefits are expected. The first benefit is the purely electrical deterministic switching of perpendicular magnetization without any assistance from an external magnetic field, since an antiferromagnet can supply an exchange-bias field, which can serve as an *effective* magnetic field. Without such a real or effective magnetic field, the switching probability is known to be around 50% due to the switching symmetry^{14,15}. In contrast, most previous experiments on the switching of perpendicular magnetization in heavy-metal based structures require the assistance of an in-plane external magnetic field to break the switching symmetry^{14,15}. The field-free switching is technologically important as the integration of external field sources

into nano-devices is harmful for scaling and thus undesirable. Yu *et al.* recently reported that the field-free switching is possible by introducing a lateral symmetry breaking in the structure, i.e., oxidation wedge¹⁸. However, this recipe requires a lateral inhomogeneity and might be inadequate for real device applications because extremely good wafer-level homogeneity of magnetic and transport properties is essential for the mass production. On the other hand, the exchange bias would allow field-free switching in laterally homogeneous structures, which should work for very small devices as proven in read sensors for hard disc drives. The second important benefit is that it provides a platform for the fundamental understanding of spin-orbit torque physics and other spin-orbit-coupling-related phenomena in antiferromagnets. In contrast to heavy metals, antiferromagnets have antiferromagnetic order, whose role and combined effect with the spin-orbit coupling on spin transport are largely unexplored. Our study of the spin-orbit torque in antiferromagnet/ferromagnet/oxide structures presented in this work could offer a step towards this rich physics.

Spin-orbit torques originating from antiferromagnets

Here we present our results for antiferromagnet/ferromagnet/oxide structures. We fabricate underlayer/CoFeB(1 nm)/MgO(1.6 nm)/Ta(2 nm) Hall bar structures (see Fig. 1a and Methods) where the perpendicular magnetic anisotropy is established in the CoFeB layer. We examine various underlayers including Ta, Ti, or IrMn (=Ir₁Mn₃). When the underlayer includes an antiferromagnet (i.e., IrMn), the perpendicular magnetic anisotropy is achieved only in very limited ranges of the CoFeB thickness so that we fix the CoFeB thickness at 1 nm, which is within such a range. As the CoFeB(1 nm)/MgO(1.6 nm)/Ta(2 nm) trilayer is common for all samples in our work, we will refer to this upper trilayer as CoFeB/MgO.

We examine the spin-orbit torque that arises when an in-plane current flows through the

layered structures. The spin-orbit torque is commonly decomposed into two mutually orthogonal vector components, i.e., a field-like torque $\mathbf{T}_F = \gamma B_F \mathbf{m} \times \mathbf{y}$ and a damping-like torque $\mathbf{T}_D = \gamma B_D \mathbf{m} \times (\mathbf{y} \times \mathbf{m})$, where γ is the gyromagnetic ratio, \mathbf{m} is the unit vector along the magnetization, \mathbf{y} is the unit vector perpendicular to both current direction (\mathbf{x}) and the direction in which the inversion symmetry is broken (\mathbf{z} , thickness direction), and B_F and B_D are the effective spin-orbit fields corresponding to field-like and damping-like torques, respectively. We perform the lock-in harmonic Hall voltage measurement^{19,20} (see Methods for details), which is commonly adopted to assess the magnitudes of the two spin-orbit torque components individually. We apply an a.c. current to generate a periodic spin-orbit torque that induces the magnetization oscillation around the equilibrium direction. The resultant oscillation of the Hall resistance combined with the a.c. current generates the second harmonic signal $V_{2\omega}$ in the Hall voltage whereas the equilibrium direction is recorded in the first harmonic signal $V_{1\omega}$. We perform the measurements for two field geometries (the external field $B = B_x$ and $B = B_y$). The sign of $V_{2\omega}$ for $B=B_x$ ($B=B_y$) represents the sign of damping-like (field-like) spin-orbit torque when the planar Hall voltage is much smaller than the anomalous Hall voltage²⁰ (see detailed equations in Supplementary Note 1) as in our samples (Supplementary Note 2, Table S1).

The lock-in measurement confirms that the antiferromagnetic IrMn layer indeed generates spin-orbit torques. Figures 1b and 1d show $V_{2\omega}$ for the Ta(5 nm)/CoFeB/MgO sample and the Ta(5 nm)/IrMn(9 nm)/CoFeB/MgO sample, respectively. In order to introduce an in-plane exchange bias in the Ta/IrMn/CoFeB/MgO sample, we anneal the sample at 190 °C in an in-plane magnetic field of 0.8 T that is the maximum field we can apply in our field-annealing set-up. The hysteresis loop shows a clear shift to the negative field direction only when the

field is applied in the x direction (Fig. 1f), which demonstrates a clear in-plane exchange bias obtained in the sample though its magnitude is about 0.5 mT, which is rather small. We observe that, by inserting an IrMn layer between Ta and CoFeB layers, the sign of $V_{2\omega}$ changes for both longitudinal ($B = B_x$) and transverse ($B = B_y$) field geometries, demonstrating the sign reversal of both field-like and damping-like spin-orbit torques. The absolute magnitude of the effective spin-orbit field for the damping-like torque of the Ta/IrMn/CoFeB/MgO sample is comparable to that of the Ta/CoFeB/MgO sample (Supplementary Note 3). We also perform the harmonic Hall voltage measurements for the samples with different underlayers, such as Ta(5 nm)/Ti(5 nm)/CoFeB/MgO sample and the Ta(5 nm)/Ti(5 nm)/IrMn(3 nm)/CoFeB/MgO sample, where we also observe a similar sign reversal of spin-orbit torque by introduction of IrMn layer (Supplementary Note 4). These results confirm unambiguously that the IrMn layer is responsible for the sign reversal of spin-orbit torques and thus acts as a spin-orbit torque source.

Field-free spin-orbit torque switching

In order to prove that the antiferromagnets make field-free spin-orbit torque switching possible by combining spin-orbit torque and exchange bias effects, we perform the switching experiment by applying current pulses (pulse width of 10 μ s). Under a positive external field B_x , we find that a positive current favours the switching from $-z$ to $+z$ direction for the Ta/CoFeB/MgO sample (Fig. 1c). In contrast, a negative current is required for the same switching direction in the Ta/IrMn/CoFeB/MgO sample (Fig. 1e). We also perform the switching experiment for the Ta/IrMn/CoFeB/MgO sample under *no* external field when the current flows in the x direction, parallel to the exchange bias (Fig. 1g). The switching direction is deterministic and the same as that of Fig. 1e, consistent with the expected

switching direction from the exchange bias (Fig. 1f). These results confirm that the IrMn layer supplies not only spin-orbit torque but also in-plane exchange bias, which enables the field-free spin-orbit torque switching.

The results in Fig. 1 provide a proof-of-principle for the active role of antiferromagnets in the field-free spin-orbit torque switching. The perpendicular switching under no field is however incomplete as indicated by black arrows in Fig. 1g. Considering that the standard spin-orbit torque sample geometry without an antiferromagnet layer suffers a similar problem if an external in-plane magnetic field is weak (Supplementary Note 5), we attribute this incomplete switching to the rather small exchange bias in our sample, which is possibly due to an insufficient magnetic field strength during the field-annealing process. We suspect that the sample annealing at higher magnetic field generates stronger exchange bias and solves the incomplete switching problem. Another option is to explore other antiferromagnet materials, which may generate higher exchange field than IrMn.

An alternative way to improve the in-plane effective field induced by the interfacial exchange coupling is to introduce another CoFeB(3 nm) layer with the in-plane anisotropy just below the IrMn layer, Ta(5 nm)/CoFeB(3 nm)/IrMn(3 nm)/CoFeB(1 nm)/MgO sample. We expect the antiferromagnetic moment can be coupled with the bottom in-plane CoFeB(3 nm) layer and the resultant antiferromagnetic order can in turn provide a stronger exchange-coupling-induced *in-plane* field for the top perpendicular CoFeB(1 nm) layer. As demonstrated in Fig. 2, we achieve complete field-free deterministic switching of perpendicular magnetization through spin-orbit torques by introducing the bottom in-plane CoFeB(3 nm) layer. We initially apply a set-field B_{set} of +0.35 T in the x direction to fully saturate the in-plane moment of the bottom CoFeB(3 nm) layer, which would set the direction

of the antiferromagnetic moment. After removing B_{set} , we apply repeated current pulses of +10 mA, 0 mA, or -10 mA (i.e., 10 mA corresponds to the current density of $4.2 \times 10^{11} \text{ A m}^{-2}$). We find that a negative (positive) current pulse preferentially switches the magnetization from $-z$ to $+z$ ($+z$ to $-z$) direction (Figs. 2b and 2d), which is the same switching direction as that of the Ta/IrMn/CoFeB/MgO sample (Fig. 1g). Therefore, a positive B_{set} establishes a positive in-plane effective field in the CoFeB(3 nm)-inserted sample. When we initially apply a negative B_{set} of -0.35 T, the exact opposite switching direction is obtained (Fig. 2e).

These results evidence that there must be a *reversible* in-plane effective magnetic field generated in the top CoFeB layer, defining the switching polarity. However, it is technically difficult to directly detect the *in-plane* effective magnetic field in the sample where the top CoFeB layer has a perpendicular magnetic anisotropy because its anisotropy field (of the order of 0.5 T) is much larger than a typical antiferromagnet-induced magnetic field (a few to tens of millitesla, mT)⁵, and the in-plane effective field reverses upon the reversal of the bottom in-plane CoFeB(3 nm) layer. In order to overcome the technical difficulty, we replace a perpendicularly magnetized top CoFeB layer with an in-plane magnetized top Co layer, which allows us to confirm that the exchange coupling between IrMn and ferromagnetic layers generates an effective in-plane magnetic field (See details in Supplementary Note 6 and 7). However this is not the only source for the in-plane effective field in the CoFeB(3 nm)-inserted sample. The second possible source is the stray field, which is however in the opposite direction to B_{set} so that it cannot explain the switching direction. The third possible source is the orange-peel coupling field originating from the bottom CoFeB(3 nm) layer.

To shed light on the main source of the in-plane effective field observed in the Ta/CoFeB(3 nm)/IrMn(3 nm)/CoFeB(1 nm)/MgO sample (IrMn-inserted sample), we

fabricate the Ta/CoFeB(3 nm)/Ta(3 nm)/CoFeB/MgO sample (Ta-inserted sample) as a test sample and compare the results between the two samples. Since the layer structure of the Ta-inserted sample is identical to that of the IrMn-inserted sample except for the replacement of the IrMn layer by the Ta layer, the second and third sources are expected to produce similar magnitudes of the in-plane effective field in both samples. Hence the difference in the net in-plane effective fields between the two samples allows one to estimate the relative importance of the first source *versus* the second and third combined.

In order to characterize the net in-plane effective field in the Ta-inserted sample, we first examine the spin-orbit torque in the Ta-inserted sample through the lock-in measurement (Fig. 3b). The signs of $V_{2\omega}$ for longitudinal ($B = B_x$) and transverse ($B = B_y$) field geometries are the same as those of the Ta/CoFeB/MgO sample. Therefore, we conclude that the spin-orbit torque in the Ta-inserted sample originates mainly from the inserted Ta layer. By the way, we observe an abrupt jump in the $V_{2\omega}$ for longitudinal ($B = B_x$) field geometry. It is nothing but the anomalous Nernst signal originating from the bottom CoFeB(3 nm) layer as evidenced by the $V_{2\omega}$ signal for the only-CoFeB(3 nm) sample without any other layers (Fig. 3c), which is irrelevant to the spin-orbit torque. We exclude a possible contribution from the spin current generated by the spin-orbit coupling effects in the bottom CoFeB(3 nm) layer because the spin-orbit torque originating from the anisotropic magnetoresistance or anomalous Hall effect has very different angular dependence²¹ from what we observe (Fig. 3b) and the Ta layer is too thick to be transparent for the spin current.

This information of the spin-orbit torque signs allows one to determine the sign of the effective in-plane field through the switching measurement. Figures 3d and 3e show the switching results of the Ta-inserted sample under B_x of +20 mT and 0 mT, respectively. In

case of $B_x = 0$, the CoFeB(3 nm) magnetization is initially set to the $+x$ direction. Under B_x of +20 mT (Fig. 3d), the switching direction is the same as that of the Ta/CoFeB/MgO sample (Fig. 1c), consistent with the sign of $V_{2\omega}$ (Figs. 1b and 3b). Interestingly, the deterministic switching persists even for $B_x=0$ (Fig. 3e), which implies the existence of an effective in-plane field. However, the switching direction for $B_x=0$ is opposite to that for $B_x=+20$ mT. It means that the sign of the effective in-plane effective field in the CoFeB(3 nm)/Ta/CoFeB/MgO sample is negative (consistent with the sign of the stray field). This effective in-plane field sign is opposite to that of the CoFeB(3 nm)/IrMn/CoFeB/MgO sample. Because these two samples have nominally the same stray and orange-peel coupling fields, this sign difference between the two samples suggests that the in-plane effective field in the CoFeB(3 nm)/IrMn/CoFeB/MgO sample is dominated by the exchange-coupling-induced field originating from the IrMn layer.

Study on the origin of antiferromagnet-induced spin-orbit torque

Finally, we discuss possible origins of spin-orbit torque in the IrMn-based structures. Existing theories for the spin-orbit-torque mechanism can be classified into two groups, i.e., the spin-orbit-coupling-dependent and the antiferromagnet-order-dependent ones. The spin-orbit-coupling-dependent mechanisms include (i) the bulk spin Hall effect^{15,22} in IrMn (possibly due to Ir) and (ii) the interfacial spin-orbit coupling (Rashba) effect^{14,23-28} at the IrMn/CoFeB interface. The antiferromagnet-order-dependent one also includes two mechanisms: (iii) the bulk inversion asymmetry of the antiferromagnetic order²⁹ and (iv) spin-wave spin current through antiferromagnets^{30,31}. A more detailed description is necessary for the mechanism (iv) because it consists of several steps. In heavy metal/antiferromagnet/ferromagnet structures, a current passing through heavy metal

generates spin-orbit torque that excites antiferromagnetic moments. This excitation in turn generates a spin-wave spin current in antiferromagnet, which is absorbed by ferromagnet via the exchange-coupling between antiferromagnet and ferromagnet.

We first attempt to differentiate mechanisms based on (i) the bulk spin Hall effect and (ii) the interfacial Rashba effect. For this purpose, we adopt the experimental method in Ref. 32 and fabricate Ta(5 nm)/Ti(5 nm)/IrMn(5 nm)/Ti(t_{Ti})/CoFeB/MgO samples where a Ti layer is inserted between the IrMn and CoFeB layers, which would diminish an interfacial effect at the IrMn/CoFeB interface. Unlike Ref. 32, where a Cu layer is inserted to diminish an interfacial effect, we choose a Ti layer instead, because the perpendicular magnetic anisotropy is not obtained for Cu-inserted structures. We note that the inserted Ti layer itself does not generate spin-orbit torque since spin-orbit torques in the Ti/CoFeB/MgO sample (with neither Ta nor IrMn) are vanishingly small (Supplementary Note 8) probably owing to the small spin-orbit coupling of Ti. We perform the harmonic Hall voltage measurement for the samples with varying Ti thickness t_{Ti} from 0 nm to 3 nm. Interestingly, we observe that the sign of spin-orbit torque changes when t_{Ti} is 3 nm (Figs. 4b and 4c). A similar sign change of spin-orbit torque is observed in IrMn(5 nm)/Ti(3 nm or 5 nm)/CoFeB/MgO samples where no underlayer is deposited below the IrMn layer (Supplementary Note 9, Fig. S11). The sign change of the spin-orbit torque in the sample with 3 nm Ti layer is confirmed by the reversal of the switching polarity as shown in Figs. 4e and 4f. On the other hand, in the Ta/Ti/CoFeB/MgO samples, the sign of spin-orbit torque does not change at a thicker Ti layer (Supplementary Note 9, Fig. S12). This difference in the sign change implies that the spin-orbit torque mechanism for IrMn would be distinctly different from that of Ta. Neither the bulk spin Hall effect nor the interfacial Rashba effect can explain the sign change in IrMn-

based samples with thicker Ti because spin-orbit torques should simply vanish at large t_{Ti} if one of these mechanisms were the origin. The mechanism (iii) (i.e., bulk inversion asymmetry of antiferromagnetic order) by itself cannot explain the sign change, because the sign of spin-orbit torque arising from this mechanism should be fixed by the inversion asymmetry.

We next check the mechanism (iv) (i.e., spin-wave spin current through antiferromagnet). We perform the harmonic Hall voltage measurement for the Ti(5 nm)/IrMn(5 nm)/CoFeB/MgO sample where no $5d$ element is present below the IrMn layer. We obtain clear spin-orbit-torque signals with the same sign of other IrMn-based structures (Supplementary Note 10). As the spin-orbit torque originating from Ti is negligible (Supplementary Fig. S10), and the magnitudes of $V_{1\omega}$ and $V_{2\omega}$ signals in the Ti/IrMn/CoFeB/MgO sample are similar to those in the Ta/Ti/IrMn/CoFeB/MgO sample (Supplementary Fig. S2), we conclude that the mechanism (iv) is not dominant in our sample. Furthermore, the mechanism (iv) cannot by itself explain the sign change of spin-orbit torque shown in Fig. 4 and Fig. S11. Therefore, the sign change of spin-orbit torque at a thicker Ti cannot be explained solely by one of existing theories, suggesting that two or more mechanisms may co-exist or another yet-unidentified mechanism may be important. We hope our results will motivate further theoretical and experimental efforts to uncover the dominant mechanism of spin-orbit torques in antiferromagnets, which would be beyond the current understanding of spin-orbit torque physics. We end this paper by emphasizing that we demonstrate field-free spin-orbit torque switching in three types of laterally homogeneous structures by utilizing an antiferromagnet, an in-plane magnetized ferromagnet, or both, which will broaden the scope of material choice and be beneficial for real device applications

utilizing the spin-orbit torque.

Note added in proof

The authors would like to state that while we were preparing the revised manuscript, we became aware that a similar work was done by other group³³.

References

1. Žutić, I., Fabian, J. & Das Sarma, S. Spintronics: fundamentals and applications. *Rev. Mod. Phys.* **76**, 323-410 (2004).
2. Duine, R. Spintronics: An alternating alternative. *Nature Mater.* **10**, 344-345 (2011).
3. Marti, X. *et al.* Room-temperature antiferromagnetic memory resistor. *Nature Mater.* **13**, 367-374 (2014).
4. Satoh, T. *et al.* Spin oscillations in antiferromagnetic NiO triggered by circularly polarized light. *Phys. Rev. Lett.* **105**, 077402 (2010).
5. Nogués, J. & Schuller, I. K. Exchange bias. *J. Magn. Magn. Mater.* **192**, 203-232 (1999).
6. Núñez, A. S., Duine, R. A., Haney, P. & MacDonald, A. H. Theory of spin torques and giant magnetoresistance in antiferromagnetic metals. *Phys. Rev. B* **73**, 214426 (2006).
7. Wei, Z. *et al.* Changing exchange bias in spin valves with an electric current. *Phys. Rev. Lett.* **98**, 116603 (2007).
8. Urazhdin, S. & Anthony, N. Effect of polarized current on the magnetic state of an antiferromagnet. *Phys. Rev. Lett.* **99**, 046602 (2007).
9. Park, B. G. *et al.* A spin-valve-like magnetoresistance of an antiferromagnet-based tunnel junction. *Nature Mater.* **10**, 347-351 (2011).
10. Wang, Y. Y. *et al.* Room-temperature perpendicular exchange coupling and tunneling anisotropic magnetoresistance in an antiferromagnet-based tunnel junction. *Phys. Rev.*

- Lett.* **109**, 137201 (2012).
11. Mendes, J. B. S. *et al.* Large inverse spin Hall effect in the antiferromagnetic metal Ir₂₀Mn₈₀. *Phys. Rev. B* **89**, 140406(R) (2014).
 12. Zhang, W. *et al.* Spin Hall effects in metallic antiferromagnets. *Phys. Rev. Lett.* **113**, 196602 (2014).
 13. Chen, H., Niu, Q. & MacDonald, A. H. Anomalous Hall effect arising from noncollinear antiferromagnetism. *Phys. Rev. Lett.* **112**, 017205 (2014).
 14. Miron, I. M. *et al.* Perpendicular switching of a single ferromagnetic layer induced by in-plane current injection. *Nature* **476**, 189-193 (2011).
 15. Liu, L., Lee, O. J., Gudmundsen, T. J., Ralph, D. C. & Buhrman, R. A. Current-induced switching of perpendicularly magnetized magnetic layers using spin torque from the spin Hall effect. *Phys. Rev. Lett.* **109**, 096602 (2012).
 16. Ryu, K.-S., Thomas, L., Yang, S.-H. & Parkin, S. Chiral spin torque at magnetic domain walls. *Nature Nanotech.* **8**, 527-533 (2013).
 17. Emori, S., Bauer, U., Ahn, S.-M., Martinez, E. & Beach, G. S. D. Current-driven dynamics of chiral ferromagnetic domain walls. *Nature Mater.* **12**, 611-616 (2013).
 18. Yu, G. *et al.* Switching of perpendicular magnetization by spin-orbit torques in the absence of external magnetic fields. *Nature Nanotech.* **9**, 548-554 (2014).
 19. Kim, J. *et al.* Layer thickness dependence of the current-induced effective field vector in Ta|CoFeB|MgO. *Nature Mater.* **12**, 240-245 (2013).
 20. Garello, K. *et al.* Symmetry and magnitude of spin-orbit torques in ferromagnetic

- heterostructures. *Nature Nanotech.* **8**, 587-593 (2013).
21. Taniguchi, T., Grollier, J. & Stiles, M. D. Spin-transfer torques generated by the anomalous Hall effect and anisotropic magnetoresistance. *Phys. Rev. Appl.* **3**, 044001 (2015).
22. Dyakonov, M. I. & Perel, V. I. Current-induced spin orientation of electrons in semiconductors. *Phys. Lett. A* **35A**, 459-460 (1971).
23. Wang, X. & Manchon, A. Diffusive spin dynamics in ferromagnetic thin films with a Rashba interaction. *Phys. Rev. Lett.* **108**, 117201 (2012).
24. Kim, K.-W., Seo, S.-M., Ryu, J., Lee, K.-J. & Lee, H.-W. Magnetization dynamics induced by in-plane currents in ultrathin magnetic nanostructures with Rashba spin-orbit coupling. *Phys. Rev. B* **85**, 180404(R) (2012).
25. Pesin, D. A. & MacDonald, A. H. Quantum kinetic theory of current-induced torques in Rashba ferromagnets. *Phys. Rev. B* **86**, 014416 (2012).
26. van der Bijl, E. & Duine, R. A. Current-induced torques in textured Rashba ferromagnets. *Phys. Rev. B* **86**, 094406 (2012).
27. Kurebayashi, H. *et al.* An antidamping spin-orbit torque originating from the Berry curvature. *Nature Nanotech.* **9**, 211-217 (2014).
28. Qiu, X. *et al.* Spin-orbit-torque engineering via oxygen manipulation. *Nature Nanotech.* **10**, 333-338 (2015).
29. Železný, J. *et al.* Relativistic Néel-order fields induced by electrical current in antiferromagnets. *Phys. Rev. Lett.* **113**, 157201 (2014).

30. Takei, S., Moriyama, T., Ono, T. & Tserkovnyak, Y. Antiferromagnet-mediated spin transfer between a metal and a ferromagnet. *Phys. Rev. B* **92**, 020409(R) (2015).
31. Moriyama, T. *et al.* Spin-transfer-torque through antiferromagnetic IrMn. arXiv:1411.4100 (2014).
32. Fan, X. *et al.* Quantifying interface and bulk contributions to spin-orbit torque in magnetic bilayers. *Nature Commun.* **5**, 3042 (2014).
33. Fukami, S., Zhang, C., DuttaGupta, S., Kurenkov, A. & Ohno, H. Magnetization switching by spin-orbit torque in an antiferromagnet/ferromagnet bilayer system. *Nature Mater.* **15**, 535-541 (2016).

Acknowledgements

The authors acknowledge R. D. McMichael, M. D. Stiles, J. McClelland, and S.-B. Choe for critical reading of the manuscript. This work was supported by Creative Materials Discovery Program through the National Research Foundation of Korea (NRF-2015M3D1A1070465). B.-G.P. acknowledges financial support from the NRF (NRF-2014R1A2A1A11051344), K.-J.L. from the NRF (NRF-2013R1A2A2A01013188), B.-C.M. from the KIST institutional program, and H.-W.L. from the NRF (NRF-2013R1A2A2A05006237), J-R.J. from the NRF (NRF-2013R1A2A2A01067144)

Author contributions

B.-G.P. and K.-J.L. planned and supervised the study. Y.-W.O. and S.C.B. fabricated devices with help from Y.M.K., H.Y.L., and C.-G.Y. Y.-W.O. and S.C.B. measured spin-orbit torques with help from K.-D.L., E.-S.P., B.-C.M., K.-S.L. and J.-R.J. K.-W.K., G. G., H.-W.L., K.-J.L. and B.-G.P. analysed the results. K.-J.L. and B.-G.P. wrote the manuscript with help of Y.M.K., K.-W.K. and H.-W.L.

Competing financial interests

The authors declare no competing financial interests.

Additional information

Supplementary information is available in the online version of the paper. Reprints and permissions information is available online at www.nature.com/reprints. Correspondence and requests for materials should be addressed to K.-J.L. and B.-G.P.

Figure captions

Figure 1 | Sign of spin-orbit torques and field-free switching in the Ta(5 nm)/IrMn(9 nm)/CoFeB/MgO sample. **a**, Schematics of the antiferromagnet/ferromagnet bilayer and Hall bar structure. The second harmonic signal $V_{2\omega}$ for **b**, the Ta(5 nm)/CoFeB/MgO sample, and **d**, the Ta/IrMn/CoFeB/MgO sample. Insets show the first harmonic signal $V_{1\omega}$. The switching experiment under B_x for **c**, the Ta/CoFeB/MgO sample, and **e**, the Ta/IrMn/CoFeB/MgO sample. The magnetization direction is monitored by measuring the anomalous Hall resistance while sweeping a pulsed current. The dotted arrows indicate the switching direction. **f**, magnetic moment versus in-plane external field of the Ta/IrMn/CoFeB/MgO sample, measured by vibrating sample magnetometer. B_{EB} is the exchange bias field established in the field-annealing direction. **g**, Field-free switching of the Ta/IrMn/CoFeB/MgO sample. The Hall bar widths of the samples are 5 μm .

Figure 2 | Field-free spin-orbit torque switching in the Ta(5 nm)/CoFeB(3 nm)/IrMn(3 nm)/CoFeB/MgO sample. **a**, A conceptual schematics for the establishment of an in-plane effective field B_{eff} induced by an external set-field B_{set} . **b**, Field-free spin-orbit torque switching in the CoFeB(3 nm)-inserted sample ($B_{set} = +0.35$ T). **c**, Anomalous Hall resistance measured with an out-of-plane magnetic field, B_z . The control of magnetization direction by the repeated current pulses of +10 mA, 0 mA, or -10 mA (i.e., 10 mA corresponds to the current density of 4.2×10^{11} A m⁻²) for **d**, $B_{set} = +0.35$ T and **e**, $B_{set} = -0.35$ T. The Hall bar width of the samples is 5 μm for **b**, **c** and 2 μm for **d**, **e**.

Figure 3 | Field-free spin-orbit torque switching in the Ta(5 nm)/CoFeB(3 nm)/Ta(3 nm)/CoFeB/MgO samples. **a**, A conceptual schematics for the establishment of an in-plane effective field B_{eff} . We note that B_{eff} in this sample is the opposite to that of Ta/CoFeB(3 nm)/IrMn/CoFeB/MgO sample (Fig. 2). **b**, The second harmonic signal $V_{2\omega}$ of Ta/CoFeB(3 nm)/Ta/CoFeB/MgO sample. Insets show the first harmonic signal $V_{1\omega}$. **c**, The second harmonic signal $V_{2\omega}$ of only-CoFeB(3 nm) sample where all other layers are excluded. Switching experiments with pulsed current for **d**, $B_x = +20$ mT and **e**, $B_x = 0$ mT. The Hall bar width of the sample is 5 μm .

Figure 4 | The sign of spin-orbit torque in the Ta(5 nm)/Ti(5 nm)/IrMn(5 nm)/Ti(t_{Ti})/CoFeB/MgO samples. **a**, Layer structure. **b**, The first harmonic signal $V_{1\omega}$ versus in-plane external field B . **c**, The second harmonic signal $V_{2\omega}$ for B parallel to the x direction (i.e., damping-like spin-orbit torque). **d**, The second harmonic signal $V_{2\omega}$ for B parallel to the y direction (i.e., field-like spin-orbit torque). **e**, **f**, Spin-orbit torque switching ($B_x = 4$ mT) for the samples with different Ti thickness of $t_{Ti}=1$ nm and $t_{Ti}=3$ nm, respectively. The Hall bar widths of the samples are 5 μm .

Methods

Sample preparation

The samples are prepared by magnetron sputtering on thermally oxidized Si substrates with base pressure of less than 4.0×10^{-6} Pa (3.0×10^{-8} Torr) at room temperature. All metallic layers are grown by d.c. sputtering with working pressure of 0.4 Pa (3 mTorr), while MgO layer is deposited by RF sputtering (150 W) from an MgO target at 1.33 Pa (10 mTorr). The composition of CoFeB is $\text{Co}_{32}\text{Fe}_{48}\text{B}_{20}$. The top Ta layer is used as a capping layer to protect the MgO layer. In order to promote the perpendicular magnetic anisotropy, samples are annealed at 150 °C for 40 min in vacuum condition, unless otherwise specified. The Hall-bar structures are fabricated by photo- or e-beam-lithography, followed by Ar ion-beam etching.

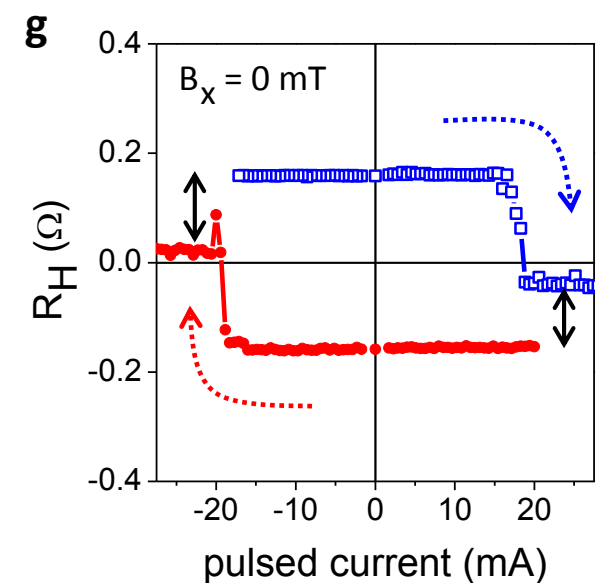
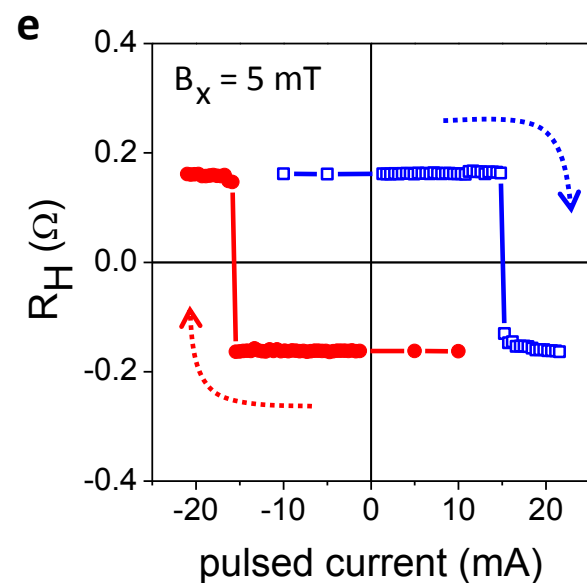
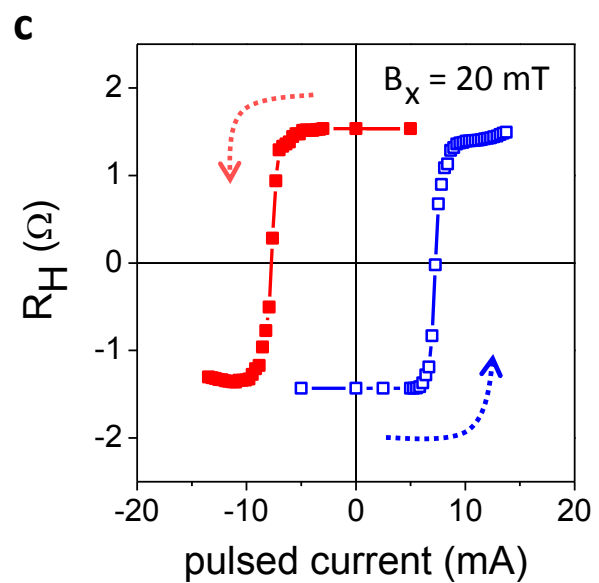
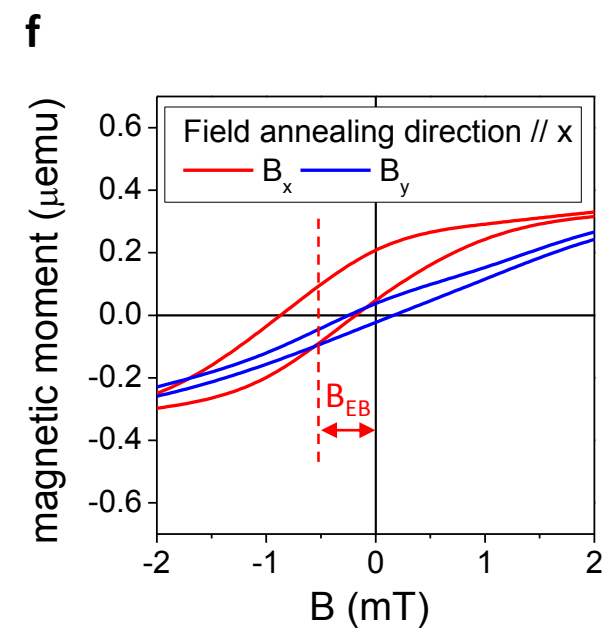
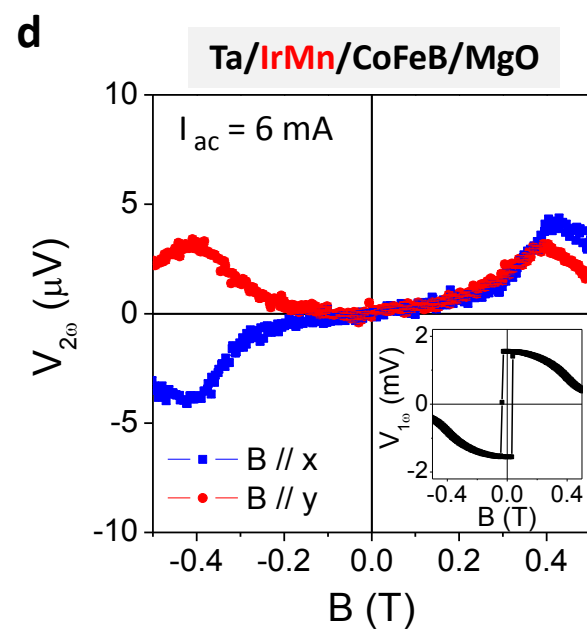
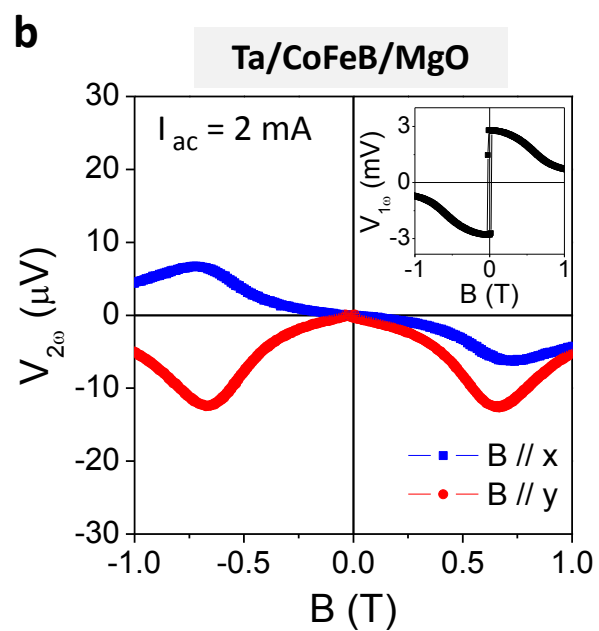
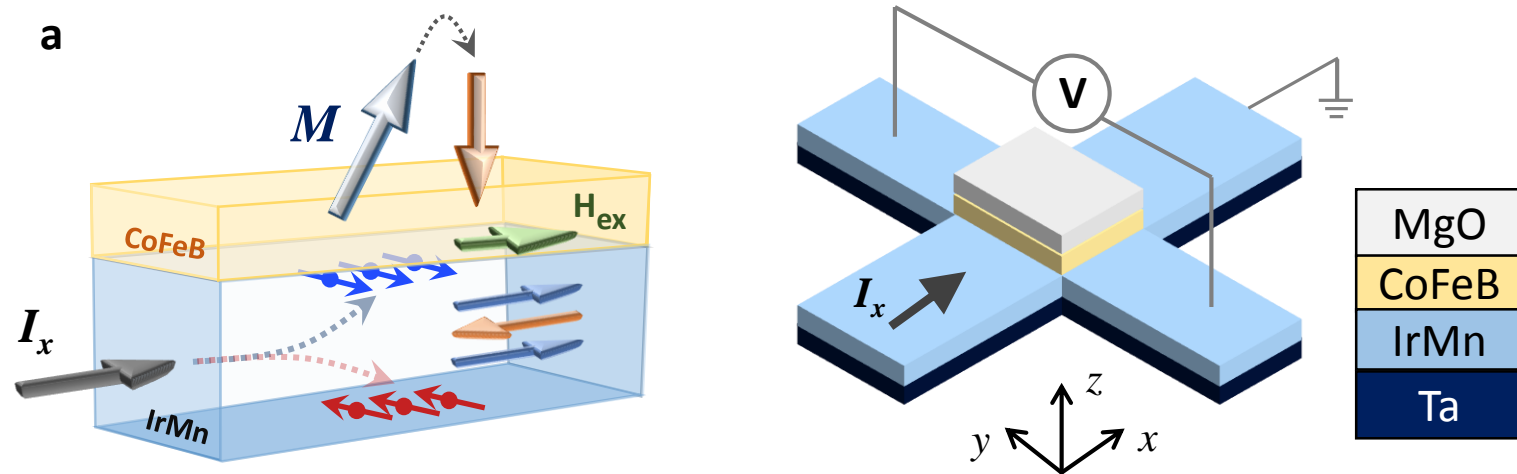
Measurements

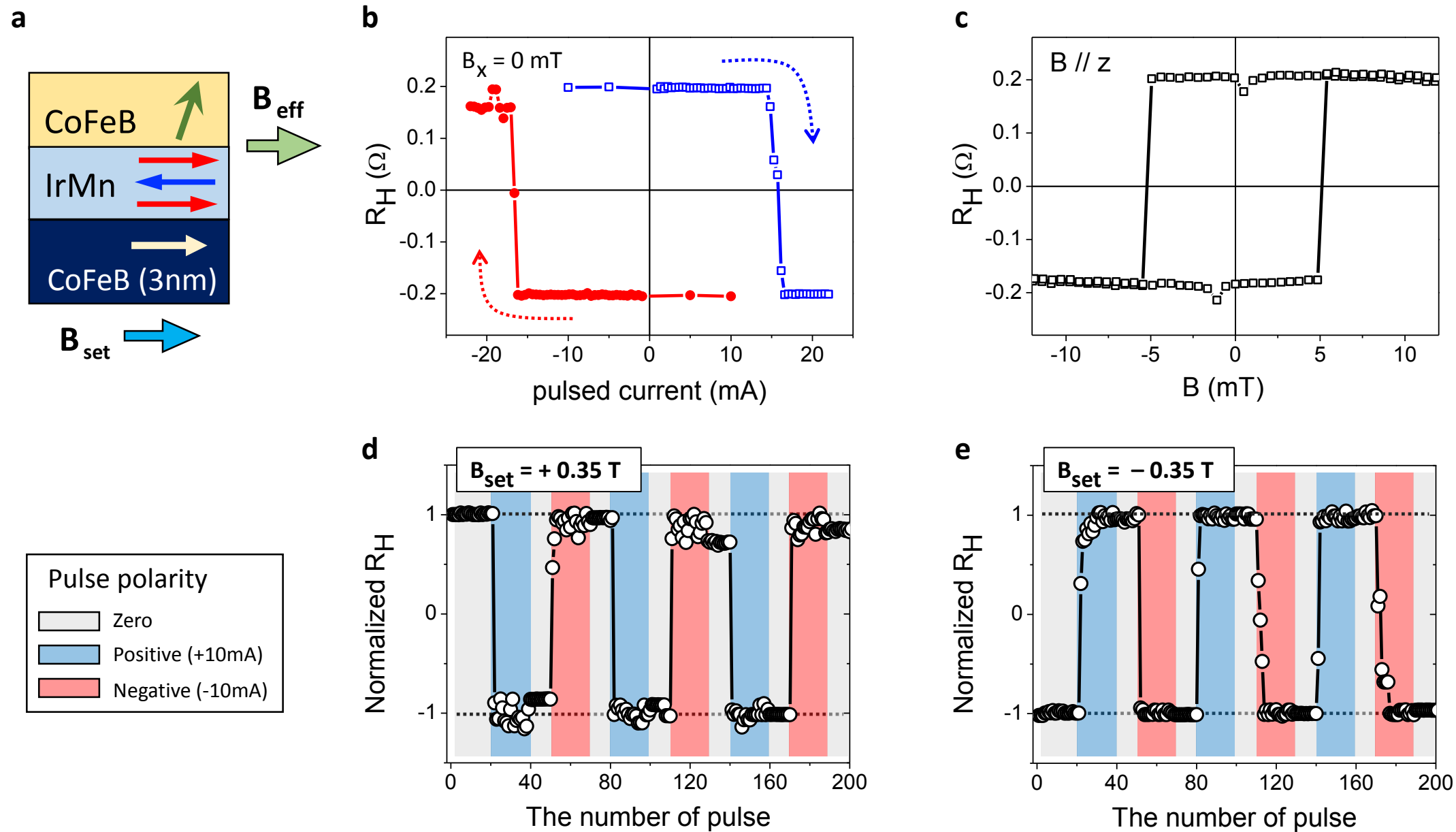
The effective magnetic fields (B_F and B_D) arising from spin-orbit torques are measured by using the harmonic lock-in technique with 2 μm to 5 μm wide Hall-bar samples. We apply an a.c. current oscillating at 50 Hz and simultaneously measure the first and second harmonic Hall voltages during the sweep of in-plane external magnetic fields, in longitudinal (B_x) or transverse (B_y) directions to the current. The switching experiments are done with 0.5 μm to 5 μm wide Hall bar structures by measuring the anomalous Hall voltage after applying a current pulse of 10 μs at each sweeping B_x or by sweeping current with a fixed B_x . All measurements are carried out at room temperature. The single standard deviation uncertainty of the lock-in harmonic Hall voltage measurements is $\pm 0.15 \mu\text{V}$. Corresponding error bars are included in the figures. In most cases, the error bars are smaller than symbols in the figures. More than three samples are measured for each type of sample; data are qualitatively

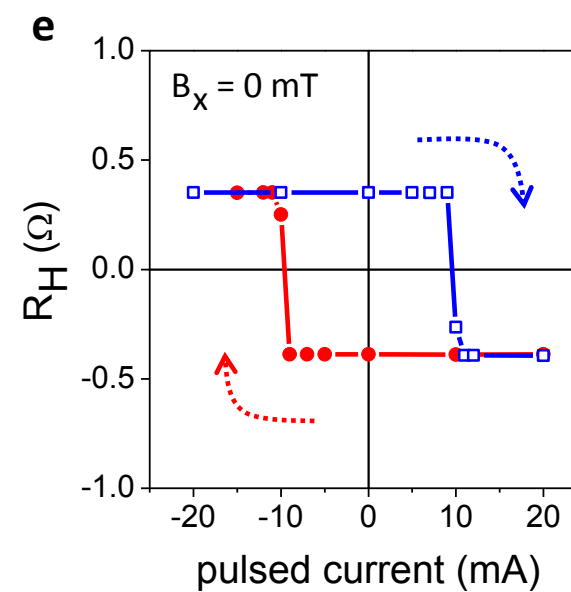
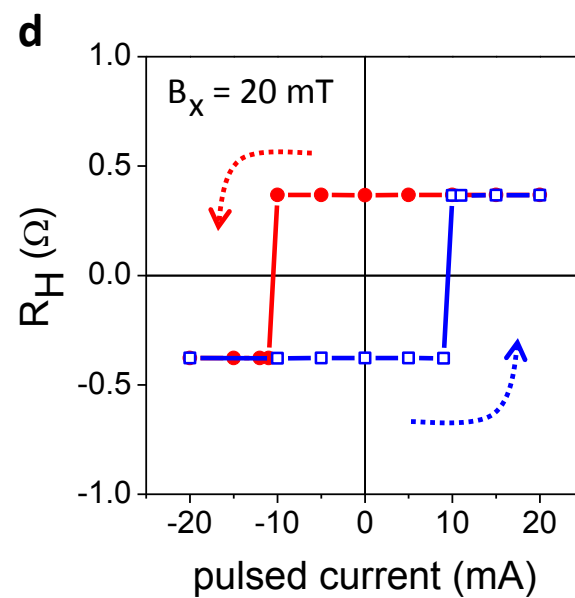
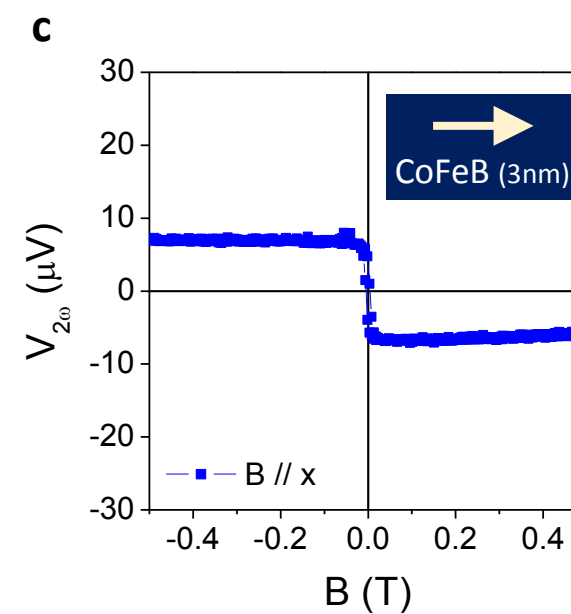
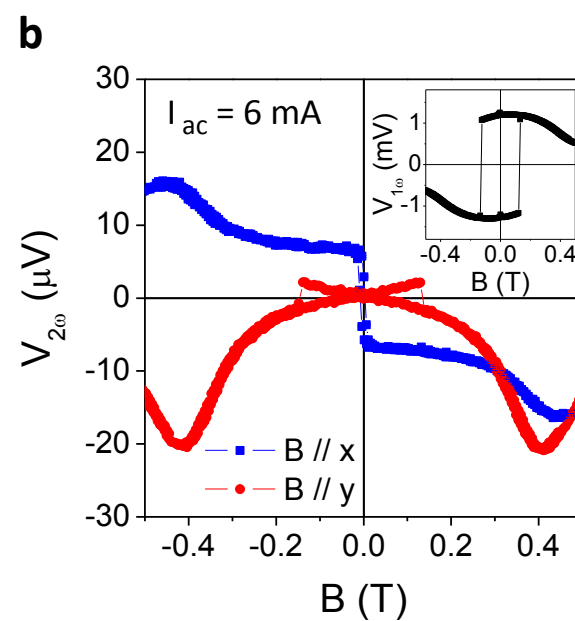
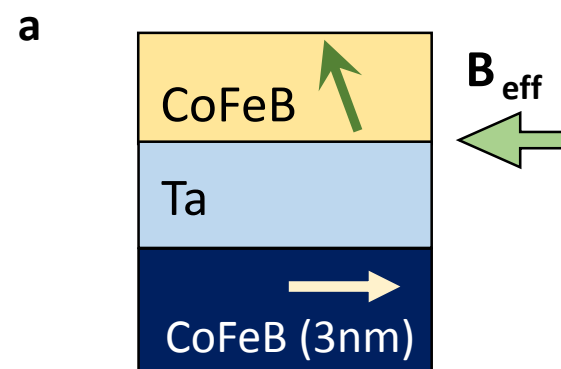
reproducible.

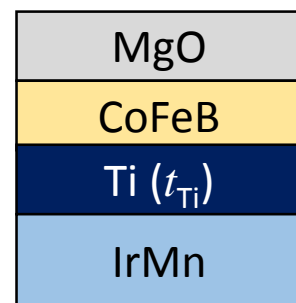
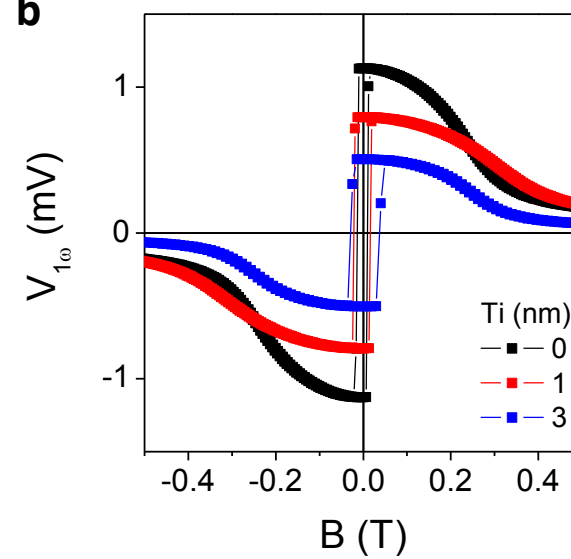
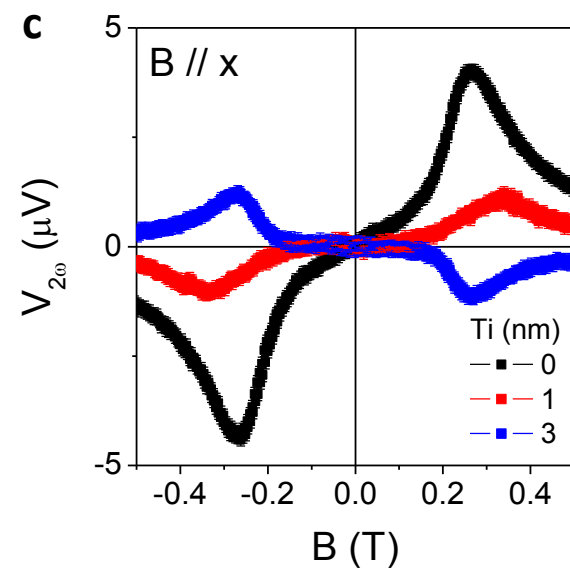
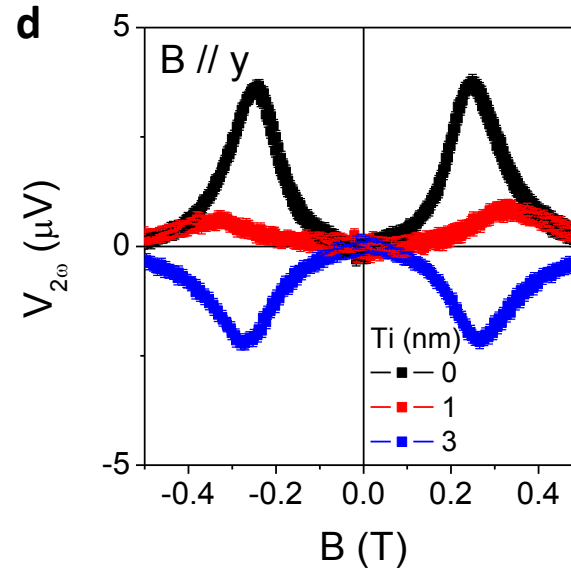
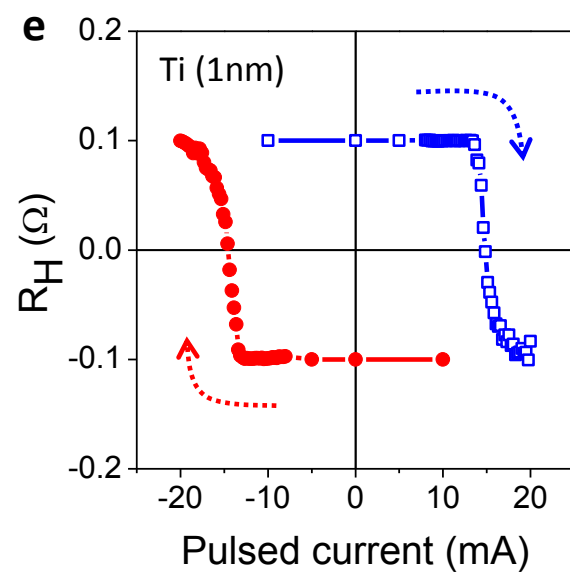
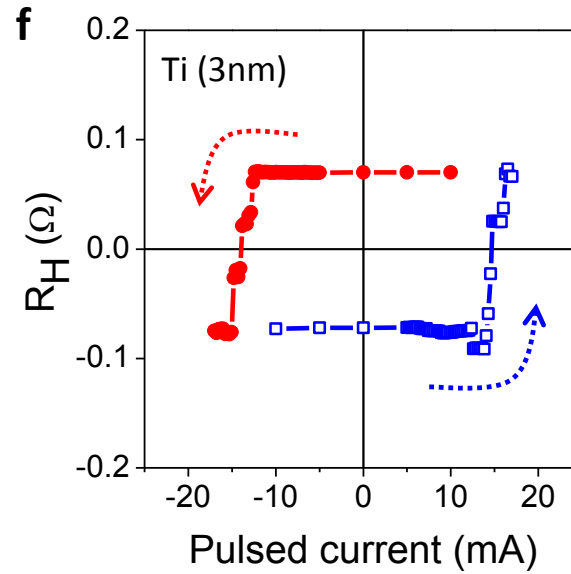
Material resistivity

The resistivity of each layer is determined by measuring the longitudinal resistance in the Hall bar structure as a function of the thicknesses of each layer. The resistivities of each layer are $(267 \pm 27) \times 10^{-8} \Omega \cdot \text{m}$ (CoFeB), $(230 \pm 33) \times 10^{-8} \Omega \cdot \text{m}$ (Ta), $(258 \pm 25) \times 10^{-8} \Omega \cdot \text{m}$ (Ti), and $(584 \pm 43) \times 10^{-8} \Omega \cdot \text{m}$ (IrMn), so that the current is not localized significantly in any one of layers.







a**b****c****d****e****f**

Supplementary Information

Field-free switching of perpendicular magnetization through spin-orbit torque in antiferromagnet/ferromagnet/oxide structures

Young-Wan Oh, Seung-heon Chris Baek, Y. M. Kim, Hae Yeon Lee, Kyeong-Dong Lee, Chang-Geun Yang, Eun-Sang Park, Ki-Seung Lee, Kyoung-Whan Kim, Gyungchoon Go, Jong-Ryul Jeong, Byoung-Chul Min, Hyun-Woo Lee, Kyung-Jin Lee and Byong-Guk Park

- Contents -

Note 1. Correlation between harmonic signals in lock-in measurements and spin-orbit torques

Note 2. Ratio of the planar Hall effect (PHE) to the anomalous Hall effect (AHE)

Note 3. Estimation of effective spin-orbit fields in Ta(5 nm)/IrMn(t_{IrMn})/CoFeB/MgO structures

Note 4. Spin-orbit torques for the Ta/Ti/CoFeB/MgO- and Ta/Ti/IrMn/CoFeB/MgO samples

Note 5. Current-induced switching in the Ta/CoFeB/MgO samples with various in-plane magnetic fields

Note 6. Effective magnetic field induced by antiferromagnetic order

Note 7. Time-Resolved magneto-optical Kerr effect experiment for the AFM/FM structure

Note 8. Spin-orbit torques in the Ti/CoFeB/MgO sample

Note 9. Effect of Ti layer thickness on the sign of spin-orbit torque in the

IrMn(5 nm)/Ti(t_{Ti})/CoFeB/MgO samples and the Ta(5 nm)/Ti(t_{Ti})/CoFeB/MgO

samples

Note 10. Spin-orbit torques of the Ti(5 nm)/IrMn(5 nm)/CoFeB/MgO sample

Note 1. Correlation between harmonic signals in lock-in measurements and spin-orbit torques

The Landau-Lifshitz-Gilbert equation including spin-orbit torque terms is given by

$$\frac{\partial \mathbf{m}}{\partial t} = -\gamma \mathbf{m} \times \mathbf{B}_{eff} + \alpha \mathbf{m} \times \frac{\partial \mathbf{m}}{\partial t} + \gamma B_F \mathbf{m} \times \mathbf{y} + \gamma B_D \mathbf{m} \times \mathbf{y} \times \mathbf{m}, \quad \dots(S1)$$

where \mathbf{B}_{eff} includes the anisotropy field, the demagnetization field, and the external field, α is the damping constant, \mathbf{y} is the unit vector perpendicular to both current direction (\mathbf{x}) and the direction in which the inversion symmetry is broken (\mathbf{z} , thickness direction), and B_F and B_D are the effective spin-orbit fields corresponding to field-like and damping-like torques, respectively. As the frequency ($= 50$ Hz) of the a.c. current is much lower than the Larmor frequency of the magnetization, one can drop time-dependent terms in Eq. (S1). Then the steady-state torque equation becomes

$$0 = -\mathbf{m} \times \mathbf{B}_{eff} + B_F \mathbf{m} \times \mathbf{y} + B_D \mathbf{m} \times \mathbf{y} \times \mathbf{m}. \quad \dots(S2)$$

Assuming $(B_x, B_y) > 0$, $(|B_F|, |B_D|) \ll |\mathbf{B}_{eff}|$, and a small amplitude change in the magnetization due to spin-orbit torques, one finds

$$V_{1\omega}^{x(y)} = V_{AHE} \sqrt{1 - \left(\frac{B_{x(y)}}{B_K} \right)^2}, \quad \dots(S3)$$

$$V_{2\omega}^x = \frac{B_x}{2B_K^2} \left(V_{AHE} \frac{B_D}{\sqrt{1 - (B_x/B_K)^2}} - V_{PHE} B_F \right), \quad \dots(S4)$$

$$V_{2\omega}^y = \frac{B_y}{2B_K^2} \left(V_{AHE} \frac{B_F}{\sqrt{1 - (B_y/B_K)^2}} - V_{PHE} B_D \sqrt{1 - (B_y/B_K)^2} \right), \quad \dots(S5)$$

where x or y describes the external field geometry, V_{AHE} and V_{PHE} are the anomalous and planar Hall voltages, respectively, and B_K is the effective perpendicular anisotropy field.

Under the same assumptions and definition of Eq. (S1), these equations are consistent with

those in literature [S1-S3]. From Eq. (S3), one finds that $V_{1\omega}^{x(y)}$ represents the equilibrium magnetization direction. On the other hand, from Eqs. (S4) and (S5), one finds that $V_{2\omega}^x$ ($V_{2\omega}^y$) is mostly determined by B_D (B_F) when $V_{\text{AHE}} > 0$ and $V_{\text{AHE}} \gg V_{\text{PHE}}$.

For the estimations of B_D and B_F from the harmonic Hall voltage signals, we follow the procedure used in Ref. S1. We exclude the anomalous Nernst effect contribution. We also correct the contributions from the planar Hall effect and the field angle (2 ~ 4 degrees from the film plane) based on a recursive procedure.

Note 2. Ratio of the planar Hall effect (PHE) to the anomalous Hall effect (AHE)

The ratio PHE/AHE of the Ta(5 nm)/IrMn(t_{IrMn})/CoFeB/MgO samples is summarized in the Table S1. Other structures also exhibit PHE/AHE < 0.1 (not shown).

Table S1 | Ratio of PHE to AHE in the Ta/IrMn(t_{IrMn})/CoFeB/MgO samples.

t_{IrMn} (nm)	PHE (Ω)	AHE (Ω)	PHE/AHE
0	0.43	1.88	0.23
3	0.029	0.90	0.032
5	0.028	0.70	0.040
7	0.024	0.58	0.041
9	0.018	0.42	0.043

Note 3. Estimation of effective spin-orbit fields in Ta(5 nm)/IrMn(t_{IrMn})/CoFeB/MgO structures

We estimate the effective spin-orbit fields B_D and B_F for the Ta(5 nm)/IrMn(t_{IrMn})/CoFeB/MgO samples with varying IrMn thickness t_{IrMn} from 0 nm to 9 nm. Figure S1 shows $V_{2\omega}$ signals and corresponding effective spin-orbit fields obtained by the procedure described in Ref. S1 (Supplementary Note 1). We find that the insertion of the IrMn layer into the stacking structure causes a sign reversal of spin-orbit torque regardless of t_{IrMn} . At a small polar angle of the magnetization, B_D of the Ta/IrMn/CoFeB/MgO sample is comparable to that of the Ta/CoFeB/MgO sample (Fig. S1c). On the other hand, the Ta/IrMn/CoFeB/MgO sample has a much smaller B_F than the Ta/CoFeB/MgO sample (Fig. S1d). In the Ta/IrMn/CoFeB/MgO sample, both B_D and B_F are insensitive to t_{IrMn} up to 7 nm and slightly decreases for sample with 9 nm IrMn.

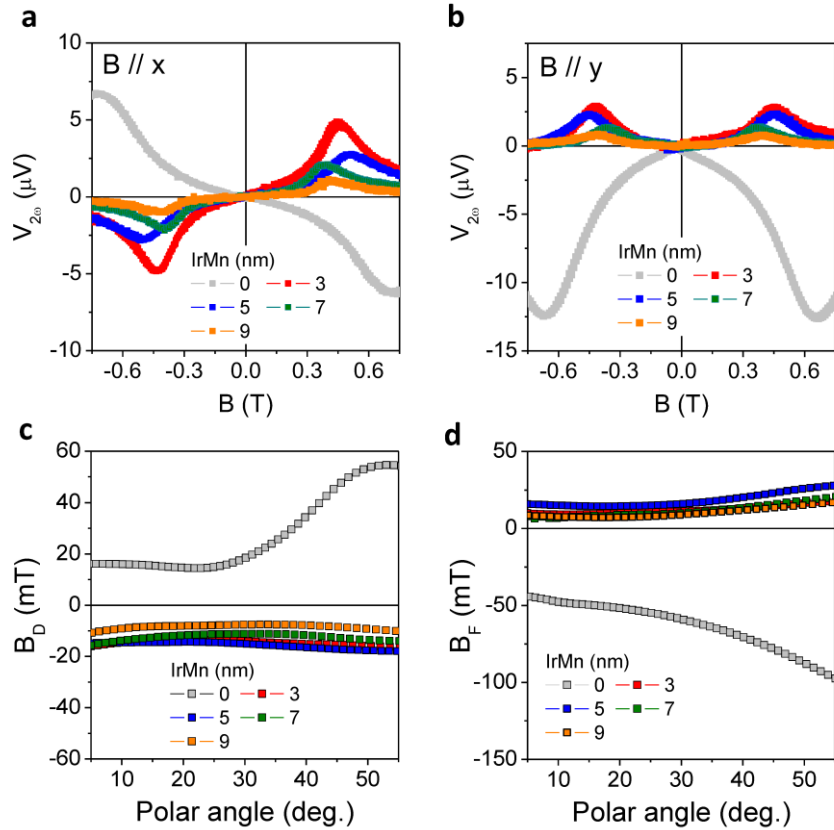


Figure S1 | Spin-orbit effective fields of the Ta(5 nm)/IrMn(t_{IrMn})/CoFeB/MgO samples.

a, The second harmonic signal $V_{2\omega}$ for the external in-plane field B parallel to the x -direction (i.e., damping-like spin-orbit torque). **b**, The second harmonic signal $V_{2\omega}$ for B parallel to the y -direction (i.e., field-like spin-orbit torque). The measurements are done with ac current of 3 mA except the sample without IrMn which is done with 2 mA. **c**, The effective field B_D (calculated from **a**) corresponding to the damping-like spin-orbit torque as a function of the polar angle of the magnetization. **d**, The effective field B_F (calculated from **b**) corresponding to the field-like spin-orbit torque as a function of the polar angle of the magnetization. Results in **c** and **d** are for the current density of $1.0 \times 10^{12} \text{ A m}^{-2}$. Zero polar angle means that the magnetization is in the z -direction.

Note 4. Spin-orbit torques for the Ta/Ti/CoFeB/MgO- and Ta/Ti/IrMn/CoFeB/MgO samples

Figures S2a and S2b show the harmonic Hall voltage measurements for the samples with a Ta(5 nm)/Ti(5 nm) underlayer of Ta(5 nm)/Ti(5 nm)/CoFeB/MgO sample and the Ta(5 nm)/Ti(5 nm)/IrMn(3 nm)/CoFeB/MgO sample. We observe a sign reversal of spin-orbit torque by introduction of IrMn layer, which is consistent with the data shown in Figs. 1b and 1d in the main text, where the samples have the Ta(5 nm) underlayer.

We perform the switching experiment by applying current pulses (pulse width 10 μs) and sweeping B_x , following the same procedure used in Ref. S4. With no current pulses (Figs. S3a and S3d), the magnetization switching is governed by the external field B_x that has a slight out-of-plane component. The switching at a large $|B_x|$ in Figs. S3c and S3e is also caused by the slight out-of-plane field. On the other hand, for a moderate B_x , the switching direction depends on the current polarity, as demonstrated in the R_H versus B_x curves for the two samples. For instance, in the Ta/Ti/CoFeB/MgO sample, a positive B_x and a positive

(negative) current favor the magnetization of $+z$ -direction ($-z$ -direction) (Figs. S3b and S3c). In contrast, an opposite current polarity is required for the same switching sequence in the Ta/Ti/IrMn/CoFeB/MgO sample (Figs. S3e and S3f). This confirms the opposite sign of spin-orbit torques which is caused by the IrMn layer in these samples irrespective of underlayers.

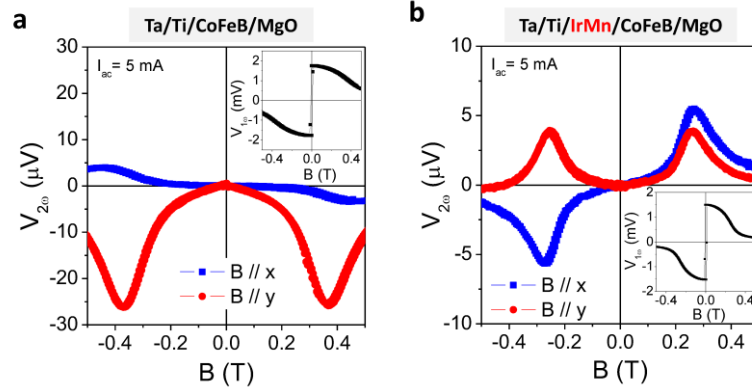


Figure S2 | The second harmonic signal $V_{2\omega}$ with Ta/Ti underlayer. a, the Ta(5 nm)/Ti(5 nm)/CoFeB/MgO sample, **b**, the Ta(5 nm)/Ti(5 nm)/IrMn(3 nm)/CoFeB/MgO sample. Insets show the first harmonic signal $V_{1\omega}$. The sign reversal by introduction of IrMn is consistent to the Fig. 1 in the main text

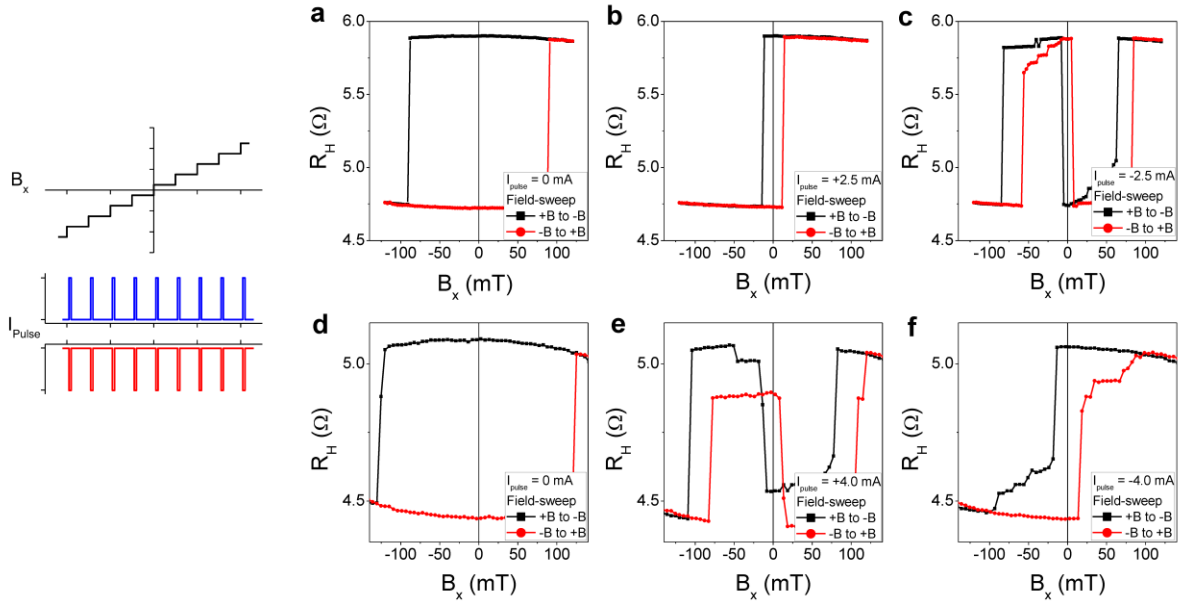


Figure S3 | Switching curves obtained with sweeping B_x and applying current pulses. The Ta(5 nm)/Ti(5 nm)/CoFeB/MgO sample: **a**, $I_{pulse} = 0 \text{ mA}$, **b**, $I_{pulse} = +2.5 \text{ mA}$, and **c**, $I_{pulse} = -2.5 \text{ mA}$. The Ta(5 nm)/Ti(5 nm)/IrMn(3 nm)/CoFeB/MgO sample: **d**, $I_{pulse} = 0 \text{ mA}$, **e**, $I_{pulse} = +4.0 \text{ mA}$, and **f**, $I_{pulse} = -4.0 \text{ mA}$.

$= +4.0$ mA, and \mathbf{f} , $I_{\text{pulse}} = -4.0$ mA. On the left, schematic diagrams describe the measurement sequence, in which the anomalous Hall voltage is detected after each current pulse while sweeping the magnetic field. The Hall bar widths of the samples are $0.5 \mu\text{m}$.

Note 5. Current-induced switching in the Ta/CoFeB/MgO samples with various in-plane magnetic fields

The complete field-free switching is not realized in the Ta/IrMn(9 nm)/CoFeB/MgO sample, which exhibits the exchange bias (Fig. 1g of the main text). We believe this is due to the fact that the exchange bias field developed in our sample is not sufficiently large (about 0.5 mT). In order to test this hypothesis, we performed spin-orbit torque switching experiment with an in-plane magnetic field and without an antiferromagnet and found that a complete switching for a sufficiently strong magnetic field gradually deforms to an incomplete switching as the field weakens. This justifies the hypothesis and implies that such an incomplete spin-orbit torque switching can be a general phenomenon when the in-plane effective field is insufficient, regardless of whether the field is supplied externally or through an exchange field of an antiferromagnet. Figure S4 shows the test experimental result for the Ta/CoFeB/MgO sample, which is a standard structure for the spin-orbit torque switching and does not contain the IrMn layer. A complete switching is accomplished under B_x of 20 mT which is sufficient to determine the switching polarity. However, when B_x is reduced below 10 mT, the switching becomes incomplete. Especially, the switching behaviour for $B_x < 1$ mT is very similar to that of samples containing the IrMn layer (Fig. 1g of the main text). These results show that the incomplete switching shown in Fig. 1g is not an exceptional feature of our IrMn samples, but a general phenomenon that is caused by an insufficient in-plane

effective magnetic field. This also suggests that a complete switching can be obtained if a larger exchange bias is achieved by optimizing the antiferromagnet/ferromagnet structures. For instance, it is known that the exchange bias of IrMn/ferromagnet structures enhances by improving the (111) texture of the IrMn layer, which can be realized by introducing an adequate underlayer such as (111)-textured ferromagnets or light elements (Cu etc.) [S5-S8]. In our study, we note however that the underlayer should satisfy two additional requirements. The first requirement is that the underlayer should be sufficiently resistive. Otherwise the underlayer will cause a significant current shunting through the underlayer and suppress the spin-orbit torque effects originating from the IrMn layer. The second requirement is that the underlayer should not degrade perpendicular anisotropy of the top CoFeB layer.

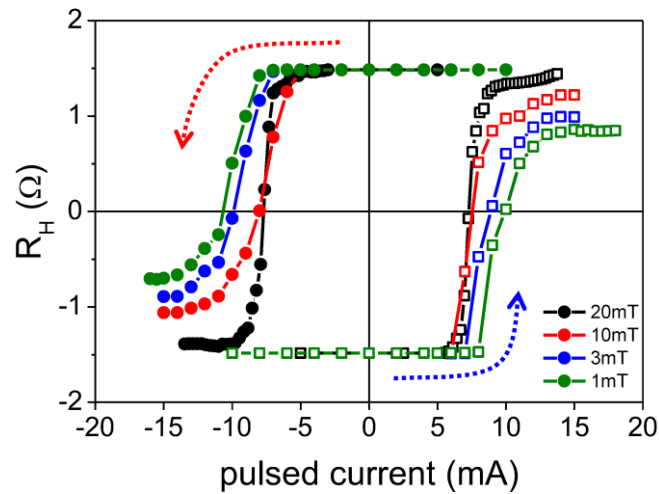


Figure S4 | Current-induced switching experiment in the Ta(5 nm)/CoFeB/MgO sample. The anomalous Hall resistance R_H is measured after each current pulse for the Ta/CoFeB/MgO sample under various in-plane magnetic fields. Experimental procedure is identical to that of Fig. 1c in the main text.

Note 6. Effective magnetic field induced by antiferromagnetic order

We first note that the exchange bias is a subset of the exchange-coupling-induced effective field since the exchange coupling at the interface of antiferromagnet(AFM)/ferromagnet(FM) manifests itself in different ways in the magnetization hysteresis loop of FM depending on the thickness of an AFM layer; a shift H_{ex} of the hysteresis loop from the origin, and an enhanced coercivity ΔH_c [S8, S9], as described in Fig. S5. We note that the emergence of either H_{ex} or ΔH_c is a direct evidence of the effective magnetic field originating from the exchange coupling at the interface [e.g., Fig. 10 of Ref. S8]. The appearance of these two effects is determined by the competition between the magnetic anisotropy of the AFM and the exchange coupling at the AFM/FM interface. The exchange bias corresponding to nonzero H_{ex} occurs when the anisotropy energy (per unit area) is larger than the interfacial exchange energy, $K_{\text{AFM}} \cdot t_{\text{AFM}} > J_{\text{ex}}$, where K_{AFM} and t_{AFM} is the magnetic anisotropy constant and the thickness of the AFM, respectively, and J_{ex} is the exchange coupling constant at the AFM/FM interface. In such case, the direction of the net AFM moment at the AFM/FM interface is not changed and the effective field is thus unidirectional, resulting in the exchange bias in the hysteresis loop of the FM layer. The exchange bias is established in our sample without the second FM, where the induced effective magnetic field has the same direction as the exchange bias as shown in Fig. 1 of the main text.

On the other hand, when the anisotropy energy is weaker than the interfacial exchange energy, $K_{\text{AFM}} \cdot t_{\text{AFM}} < J_{\text{ex}}$, the direction of the AFM moment reverses upon the reversal of the coupled FM moment [S10, S11]. Consequently, the direction of the exchange-coupling-induced effective magnetic field is reversed upon the reversal of the FM layer and the effective field is thus uniaxial. This uniaxial effective field results in the enhanced coercivity without exhibiting the exchange bias (or loop shift). This is generally observed for a thin

AFM or for a high temperature where the K_{AFM} is reduced. We note that this uniaxial effective field is also a manifestation of the interfacial exchange coupling between AFM and FM, and thus evidences the active role of AFM. This uniaxial effective field explains results of the Ta/CoFeB(3 nm)/IrMn(3 nm)/CoFeB(1 nm)/MgO samples shown in Fig. 2 of the main text, where the field-free switching is achieved and the switching polarity changes its sign upon the reversal of the bottom CoFeB layer. This points out that there must be a *reversible* in-plane effective magnetic field generated in the top CoFeB layer, which determines the switching polarity.

We next present the additional experimental results in order to demonstrate that the thin AFM IrMn layer in the Ta/CoFeB(3 nm)/IrMn(3 nm)/CoFeB(1 nm)/MgO sample indeed generates an in-plane effective field through the interfacial exchange coupling. It is technically difficult to directly detect the *in-plane* effective magnetic field in the sample where the top CoFeB layer has perpendicular anisotropy because its anisotropy field (of the order of 0.5 T) is much larger than a typical AFM-induced effective magnetic field (a few to tens of millitesla, mT). In order to overcome this technical difficulty, we replace a perpendicularly magnetized top CoFeB layer with an in-plane magnetized top Co layer and measure H_{ex} and ΔH_c . This replacement is made to clearly observe the switching of each in-plane layer (i.e., H_c of Co \gg H_c of CoFeB). We also measure a magnetization curve of Ta(5 nm)/CoFeB(3 nm)/Ta(3 nm)/Co(3 nm) layer as a control sample.

Figure S6a shows a magnetization hysteresis curve of the Ta(5 nm)/CoFeB(3 nm)/Ta(3 nm)/Co(3 nm), together with magnetization hysteresis curves of a single Ta(3 nm)/CoFeB(3 nm) and Ta(3 nm)/Co(3 nm) layer measured at room temperature. For the CoFeB/Ta/Co sample, the magnetization switches at two different magnetic fields, which correspond to the coercivities of the CoFeB and Co layers, respectively. The larger switching field corresponds

to H_c of Co layer. We observe that H_c of Co layer in the CoFeB/Ta/Co sample (indicated by a blue arrow) is almost the same as that in the Co-only sample (indicated by a red arrow). This similarity is expected because the AFM layer is absent in the CoFeB/Ta/Co sample and thus an effective field originating from the interfacial exchange coupling is absent either.

As shown in Fig. S6b, on the other hand, H_c of Co layer in Ta(5 nm)/CoFeB(3 nm)/IrMn(3 nm)/Co(3 nm) sample (indicated by a blue arrow) is substantially larger than that in the Co-only sample (indicated by a red arrow). This result clearly demonstrates that the IrMn layer inserted between the CoFeB and Co layers results in ΔH_c due to the interfacial exchange coupling. Since a clear shift of the loop is not observed, we conclude that the sample satisfies the condition of $K_{\text{AFM}} \cdot t_{\text{AFM}} < J_{\text{ex}}$ at room temperature.

We further confirm that the antiferromagnetic order is present in the IrMn layer and the consequent interfacial exchange coupling is the origin of the effective magnetic field by examining magnetization curves of the IrMn-inserted and the control samples after a field-cooled procedure from room temperature to 100 K with a magnetic field of +0.7 T and -0.7 T. We expect that the exchange bias field H_{ex} could be developed by lowering the temperature because the anisotropy constant K_{AFM} becomes greater at a lower temperature. Figures S7a and S7b clearly show that the opposite shifts of the positive and negative field-cooled curves (measured at 100 K) appear only in the IrMn-inserted sample. This exchange bias effect indeed demonstrates the existence of the antiferromagnetic order and the exchange coupling at the IrMn/Co interface. Moreover, we measure hysteresis loops of the CoFeB/IrMn/Co, CoFeB/Ta/Co, and Co-only samples at various temperatures ranging from 100 K to 450 K (Fig. S8a-c). The coercivity enhancement sustains up to 400 K whereas the exchange bias diminishes at around 250 K (Figs. S8d, e). This demonstrates that the antiferromagnetic order formed in the IrMn(3 nm) layer induces an effective magnetic field at the top surface of the IrMn layer. These results, a finite ΔH_c and negligible H_{ex} at the room temperature, are also

consistent with the field-free switching in the CoFeB(in-plane)/IrMn/CoFeB(perpendicular) samples, where the switching polarity is reversed upon the switching of in-plane CoFeB layer.

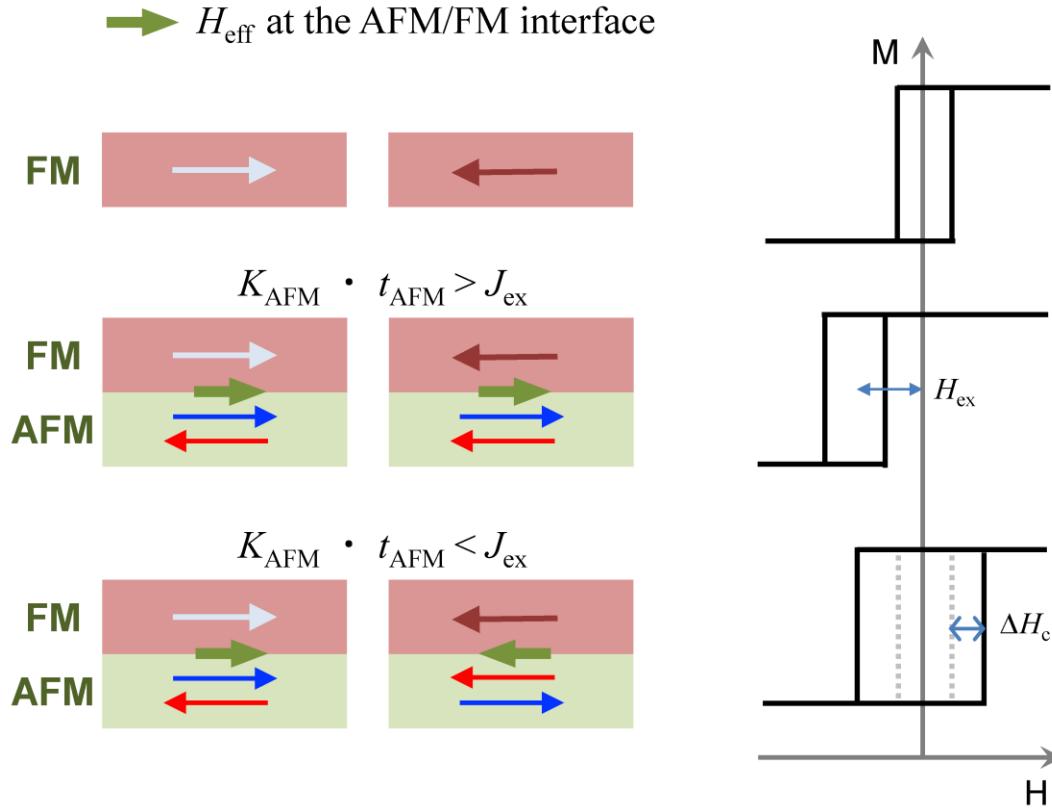


Figure S5 | Schematic description of exchange interaction of antiferromagnet (AFM)/ferromagnet (FM) structure. Magnetic configuration and corresponding magnetization curve of (top row) a single FM layer, (middle row) a FM/AFM bilayer for $K_{\text{AFM}} \cdot t_{\text{AFM}} > J_{\text{ex}}$, and (bottom row) a FM/AFM bilayer for $K_{\text{AFM}} \cdot t_{\text{AFM}} < J_{\text{ex}}$. Here, K_{AFM} and t_{AFM} are the magnetic anisotropy constant and the thickness of the AFM, respectively, and J_{ex} is the exchange coupling constant at the AFM/FM interface. Green arrows correspond to the direction of the in-plane effective field at the interface of the AFM/FM, which is caused by the interfacial exchange coupling.

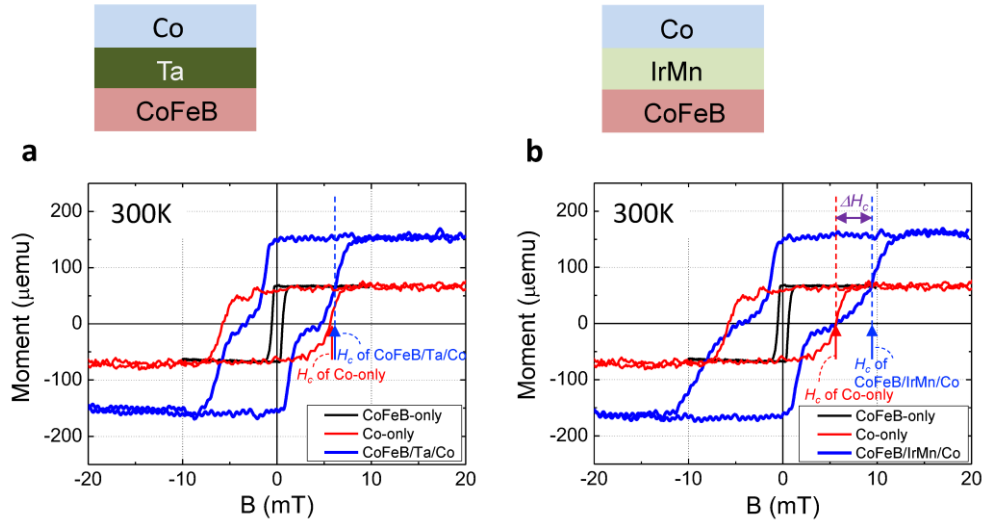


Figure S6 | Magnetization hysteresis curves in the Ta/CoFeB(3 nm)/IL(3 nm)/Co(3 nm) samples at 300K. The interlayer IL is either Ta or IrMn. **a, b**, Magnetization curves of Ta/CoFeB/Ta/Co and Ta/CoFeB/IrMn/Co, respectively. The black (red) graph represents the magnetization curves of a single CoFeB (Co) layer. The arrow indicates the coercivity of Co in each sample.

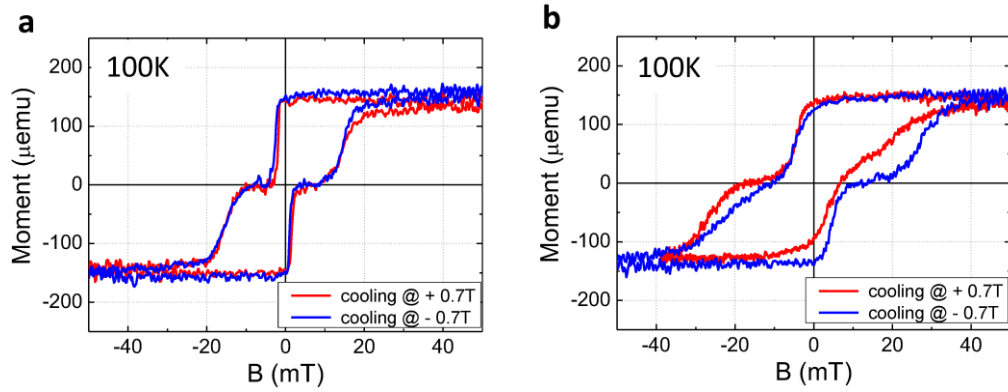


Figure S7 | Magnetization hysteresis curves in the Ta/CoFeB(3 nm)/IL(3 nm)/Co(3 nm) samples at 100K after field cooling. **a, b**, Magnetization curves of the Ta/CoFeB/Ta/Co and Ta/CoFeB/IrMn/Co samples measured at 100 K after field-cooling with a magnetic field of +0.7 T (red) and -0.7 T (blue), respectively.

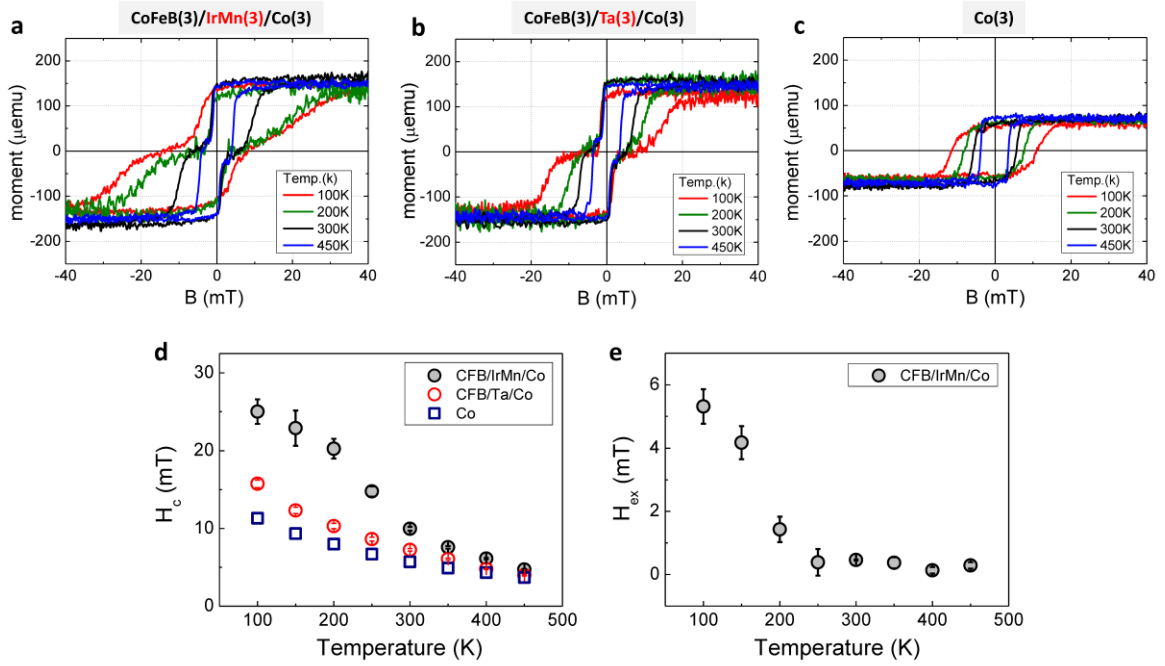


Figure S8 | Temperature dependence of the magnetization curves. Magnetization curve of each sample is measured at different temperatures ranging from 100 K to 450 K. **a**, Ta(5 nm)/CoFeB(3 nm)/IrMn(3 nm)/Co(3 nm) sample. **b**, Ta(5 nm)/CoFeB(3 nm)/Ta(3 nm)/Co(3 nm) sample. **c**, single Co(3 nm) layer. **d**, Coercivity of Co in each sample as a function of the measurement temperature. **e**, Exchange bias of Co in Ta(5 nm)/CoFeB(3 nm)/IrMn(3 nm)/Co(3 nm) sample as a function of the measurement temperature.

Note 7. Time-resolved magneto-optical Kerr effect experiment for the AFM/FM structure

We performed an additional experiment of time-resolved magneto-optical Kerr effect (TRMOKE), which allows us to investigate the effect of AFM on dynamic behaviours of FM such as effective Gilbert damping constant α and ferromagnetic resonance frequency f . It is known that these properties are modified by adjacent AFM when the exchange coupling is present at the AFM/FM interface [S12-S14].

Figure S9a shows a schematic TRMOKE measurement. An external magnetic field H is applied at an angle of 15° with respect to the sample plane to suppress domain formation [S15], and a pump laser pulse ($\Delta t = 0$) is then used to induce spin precession in the sample, since the laser heating changes the anisotropy K_{eff} and magnetization M , thereby altering the equilibrium M -orientation θ . After heating ($\Delta t > 0$), M starts to precess around its equilibrium direction and dissipate the excited energy via Gilbert damping and the restoration of K_{eff} and M . The polar component (M_z) of the precession is measured from the change in the polarization of the reflected probe beam with delay time Δt using a balanced detection technique. The probe (pump) beam has a central wavelength of 400 (800) nm, an average power of 40 μW (6 mW), and a repetition rate of 82 MHz.

The measured TRMOKE signal is shown in Fig. S9b for CoFeB(3 nm), Co(3 nm), CoFeB(3 nm)/Ta(3 nm)/Co(3 nm), and CoFeB(3 nm)/IrMn(3 nm)/Co(3 nm) samples. Note that all samples have a common Ta (5 nm) underlayer. The CoFeB and Co samples are used to identify α and f of an individual layer of CoFeB and Co, and the CoFeB/Ta/Co sample is used to estimate the effect of interlayer coupling between top Co and bottom CoFeB layers. By comparison of the result of those samples with that of the CoFeB/IrMn/Co sample, we examine the exchange coupling effect from AFM IrMn. To analyse the data, TRMOKE traces are fitted with the following phenomenological formula considering resonance frequencies of CoFeB and Co layers [S15],

$$-\frac{\Delta M_z}{M_z} = A_0 + A_2 e^{-\frac{\Delta t}{\tau_e}} + \frac{A_3}{\sqrt{1 + \frac{\Delta t}{t_0}}} + A_1 e^{-\frac{\Delta t}{\tau_1}} \sin(2\pi f_1 \Delta t + \varphi_1) + A_2 e^{-\frac{\Delta t}{\tau_2}} \sin(2\pi f_2 \Delta t + \varphi_2),$$

...(S6)

where τ is the relaxation time of the precession and subscript 1(2) denotes to CoFeB (Co). The first term A_0 is the non-magnetic background, and the second term represents relaxation of the electron temperature with an equilibration time τ_e . The third term expresses one

dimensional heat diffusion with the absorption temporal profile t_0 . Precessional magnetization motion is described by the last two terms, where $A_{1,2}$ is the excited precession amplitude. From the fitting curves depicted as lines in Fig. S9b, the material parameters are obtained by the following relation:

$$\alpha_1 = (2\pi f_1 \tau_1)^{-1}, \alpha_2 = (2\pi f_2 \tau_2)^{-1}, \alpha_{12} = \frac{A_1 \alpha_1 + A_2 \alpha_2}{A_1 + A_2}, \quad \dots (S7)$$

where $\alpha_{1,2}$ is the effective Gilbert damping constants. As the amount of actual energy dissipation in the multilayer system depends not only on damping constant but also on the excited amplitude of each precession, the combined damping constant weighted by the excited precession amplitude, α_{12} is considered. This is also applied to an individual layer where α_{12} becomes α_1 or α_2 for A_2 and $A_1 = 0$, respectively. The enhanced α_{12} indicates that the strong coupling exists as a damping channel, the exchange coupling in our structure for example. In addition to α_{12} , coupling of CoFeB and Co layers changes their distinct resonance frequency f_1 and f_2 , and their difference $\Delta f = |f_1 - f_2|$. For instance, if strong (exchange) coupling exists, Δf reduces notably from the uncoupled distinct resonance behaviour.

The fitted parameters are summarized in Table S2. As compared to results in the single FM, α_{12} (Δf) increases (decreases) in the CoFeB/Ta/Co and CoFeB/IrMn/Co samples, indicating interlayer coupling between FM layers. Moreover, for the sample with AFM IrMn, damping constant α_{12} and frequency difference Δf are pronouncedly modified, indicating an additional strong coupling between FM layers probably due to exchange interaction with AFM. These results clearly demonstrate that the exchange coupling exists at the IrMn(3 nm)/FM interfaces.

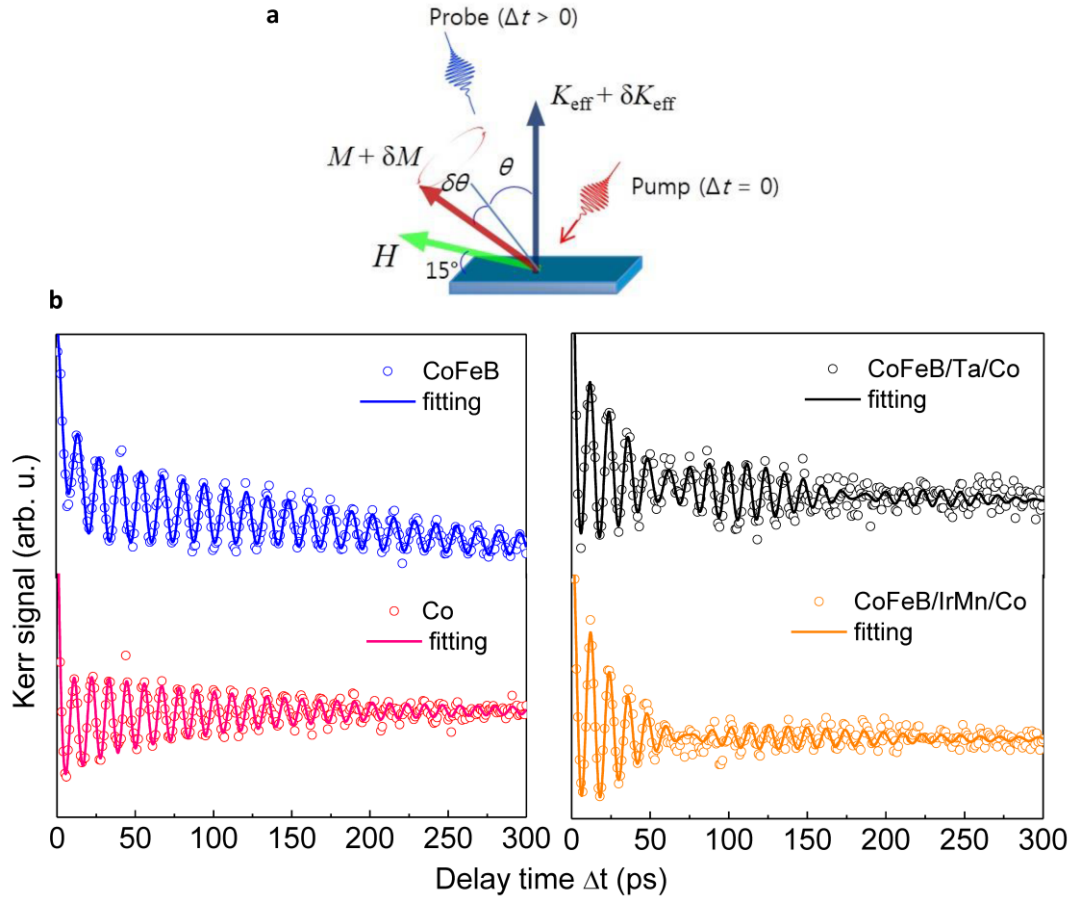


Figure S9 | Time-resolved magneto-optical Kerr effect (TRMOKE) signal. **a**, Schematic TRMOKE measurement and the excitation process. **b**, TRMOKE signal in CoFeB(3 nm), Co(3 nm), CoFeB(3 nm)/Ta(3 nm)/Co(3 nm), and CoFeB(3 nm)/IrMn(3 nm)/Co(3 nm) samples, when $H = 2.24$ T.

Table S2 | Precession amplitude (A), resonance frequency (f), and effective Gilbert damping constant (α) of CoFeB, Co, CoFeB/Ta/Co, and CoFeB/IrMn/Co samples obtained from Figure S8.

	CoFeB	Co	CoFeB/Ta/Co	CoFeB/IrMn/Co
A_1	1.32 ± 0.05		6.62 ± 0.47	1.10 ± 0.22
f_1 (GHz)	74.5 ± 0.10		80.8 ± 0.20	81.2 ± 0.30
α_1	0.010 ± 0.001		0.023 ± 0.002	0.012 ± 0.003
A_2		1.68 ± 0.05	2.94 ± 0.41	2.61 ± 0.23
f_2 (GHz)		89.2 ± 0.10	89.1 ± 0.20	85.9 ± 0.30
α_2		0.016 ± 0.001	0.016 ± 0.003	0.043 ± 0.005
α_{12}	0.010 ± 0.001	0.016 ± 0.001	0.021 ± 0.002	0.034 ± 0.004
Δf (GHz)	14.7 ± 0.2		8.3 ± 0.4	4.7 ± 0.6

Note 8. Spin-orbit torques in the Ti/CoFeB/MgO sample

Figures S10a and S10b respectively show $V_{1\omega}$ and $V_{2\omega}$ signals of the Ti(5 nm)/CoFeB/MgO sample where no other layers except for the Ti layer is present as a underlayer of CoFeB. For comparison, $V_{1\omega}$ and $V_{2\omega}$ signals of the Ta/Ti/IrMn/CoFeB/MgO sample are shown in Figs. S10c and S10d, respectively. Given the similar magnitude of $V_{1\omega}$ signal for the two types of samples, much smaller $V_{2\omega}$ signals for the Ti/CoFeB/MgO sample than for the Ta/Ti/IrMn/CoFeB/MgO sample show that spin-orbit torques originating from the Ti layer are negligible.

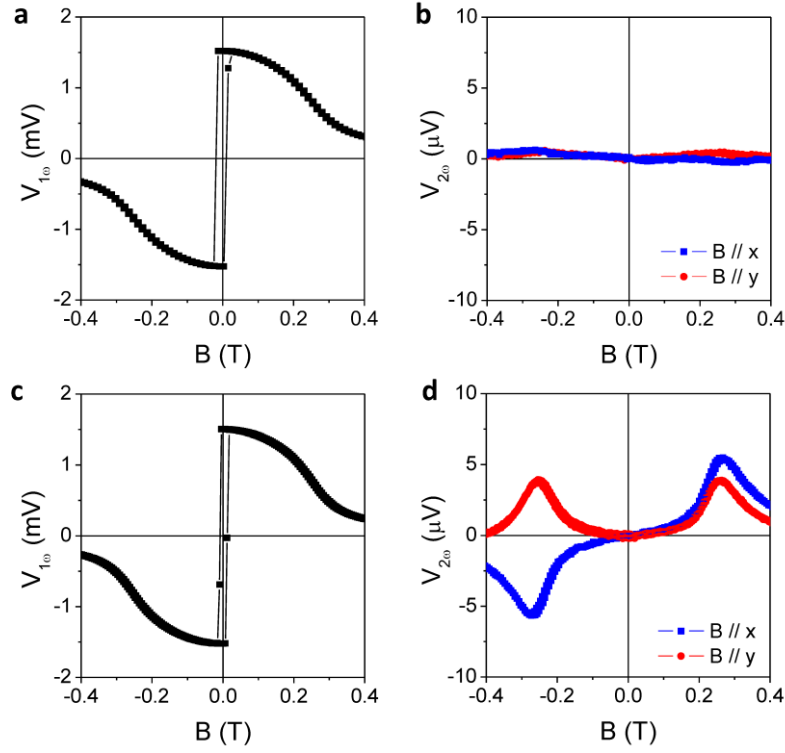


Figure S10 | The harmonic spin-orbit torque signals. a, $V_{1\omega}$ and b, $V_{2\omega}$ signals for the Ti/CoFeB/MgO sample. c, $V_{1\omega}$ and d, $V_{2\omega}$ signals for the Ta/Ti/IrMn/CoFeB/MgO sample.

Note 9. Effect of Ti layer thickness on the sign of spin-orbit torque in the IrMn(5 nm)/Ti(t_{Ti})/CoFeB/MgO samples and the Ta(5 nm)/Ti(t_{Ti})/CoFeB/MgO samples

Figure S11 shows $V_{1\omega}$ and $V_{2\omega}$ signals of the IrMn/Ti/CoFeB/MgO samples with varying the thickness of a Ti layer (t_{Ti}) from 1 nm to 5 nm. In this structure, we could not obtain the perpendicular magnetic anisotropy of CoFeB for $t_{\text{Ti}} = 0$ nm. The damping-like spin-orbit torque (Fig. S11b: $B // x$) changes its sign when $t_{\text{Ti}} = 3$ nm and 5 nm. The sign of $V_{2\omega}$ signal for the field-like spin-orbit torque (i.e., $B // y$) in the IrMn/Ti($t_{\text{Ti}} = 5$ nm)/CoFeB/MgO sample is clearly negative, consistent with that in the Ta/Ti/IrMn/Ti($t_{\text{Ti}} = 3$ nm)/CoFeB/MgO sample, whereas $V_{2\omega}$ signal for the field-like spin-orbit torque in the IrMn/Ti($t_{\text{Ti}} = 1$ nm or

3 nm)/CoFeB/MgO samples are negligible (not shown). In contrast, the sign of spin-orbit torque does not change with t_{Ti} in the Ta/Ti/CoFeB/MgO samples (Fig. S12).

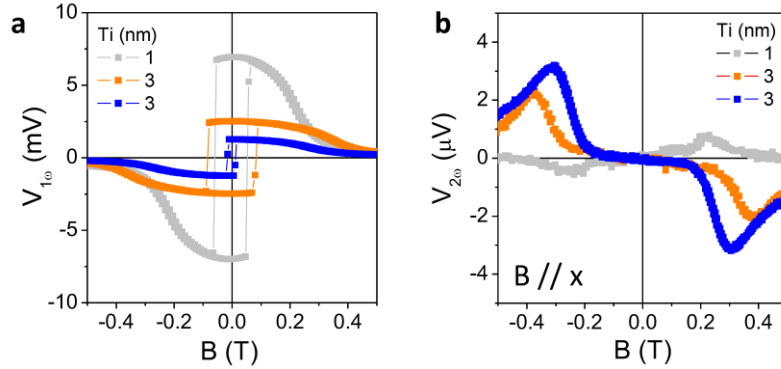


Figure S11 | The harmonic spin-orbit torque signals. a, $V_{1\omega}$ and b, $V_{2\omega}$ signals for the IrMn/Ti/CoFeB/MgO samples with varying the thickness of a Ti layer for $B // x$.

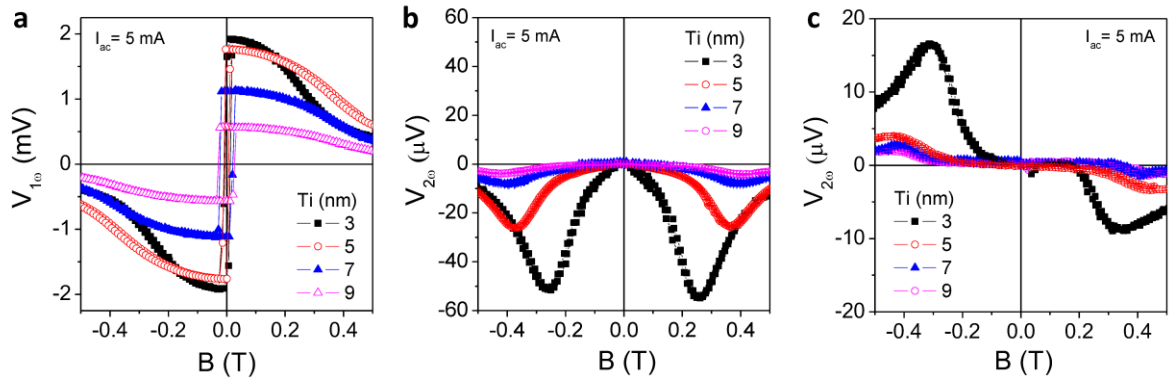


Figure S12 | The harmonic spin-orbit torque signals. a, $V_{1\omega}$ and b, c, $V_{2\omega}$ signals for the Ta/Ti/CoFeB/MgO samples with varying the thickness of a Ti layer for b, $B // y$ and c, $B // x$.

Note 10. Spin-orbit torques of the Ti(5 nm)/IrMn(5 nm)/CoFeB/MgO sample

Figures S13a and S13b show $V_{1\omega}$ and $V_{2\omega}$ signals of the Ti/IrMn/CoFeB/MgO sample where no 5d element is below the IrMn layer, respectively. For comparison, $V_{1\omega}$ and $V_{2\omega}$ signals of the Ta/Ti/IrMn/CoFeB/MgO sample are shown in c and d, respectively. The similar magnitudes of $V_{1\omega}$ and $V_{2\omega}$ signals for the two types of samples show that both damping-like

and field-like spin-orbit torques are similar in these samples.

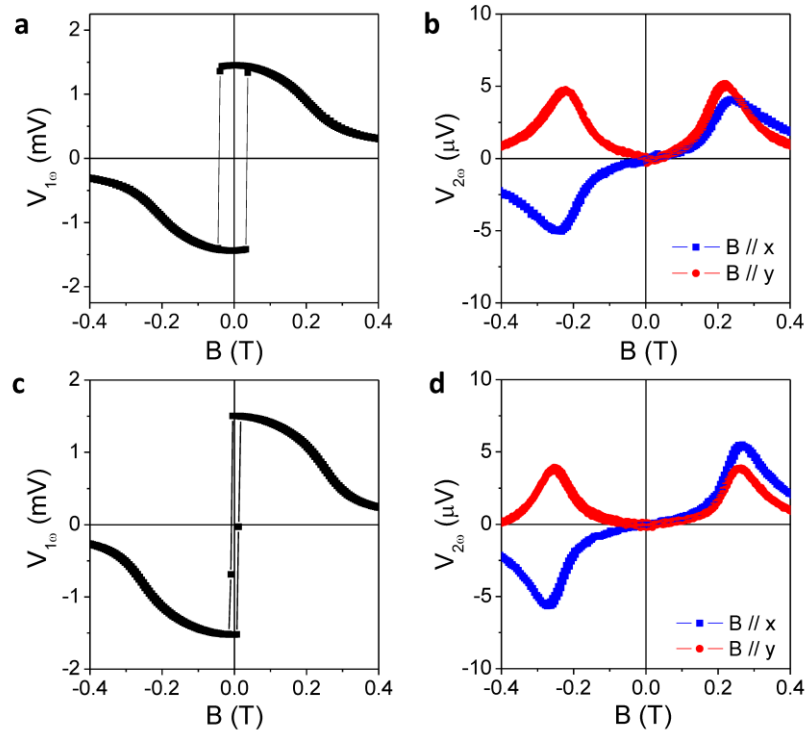


Figure S13 | The harmonic spin-orbit torque signals. **a**, $V_{1\omega}$ and **b**, $V_{2\omega}$ signals for the Ti/IrMn/CoFeB/MgO sample. **c**, $V_{1\omega}$ and **d**, $V_{2\omega}$ signals for the Ta/Ti/IrMn/CoFeB/MgO sample.

Supplementary References

- [S1] Garello, K. *et al.* Symmetry and magnitude of spin-orbit torques in ferromagnetic heterostructures. *Nature Nanotech.* **8**, 587–593 (2013).
- [S2] Qiu, X. *et al.* Angular and temperature dependence of current induced spin-orbit effective fields in Ta/CoFeB/MgO nanowires. *Sci. Rep.* **4**, 4491 (2014).
- [S3] Hayashi, M., Kim, J., Yamanouchi, M. & Ohno, H. Quantitative characterization of the spin-orbit torque using harmonic Hall voltage measurements. *Phys. Rev. B* **89**, 144425 (2014).
- [S4] Miron, I. M. *et al.* Perpendicular switching of a single ferromagnetic layer induced by in-plane current injection. *Nature* **476**, 189–193 (2011).
- [S5] Pakala, M., Huai, Y., Anderson, G. & Miloslavsky, L. Effect of underlayer roughness, grain size, and crystal texture on exchange coupled IrMn/CoFe thin films. *J. Appl. Phys.* **87**, 6653 (2000).
- [S6] Castro, I. L. *et al.* The role of the (111) texture on the exchange bias and interlayer coupling effects observed in sputtered NiFe/IrMn/Co trilayers. *J. Appl. Phys.* **113**, 203903 (2013).
- [S7] Aley, N. P. *et al.* Texture Effects in IrMn/CoFe Exchange Bias Systems. *IEEE Trans. Magn.* **44**, 2820–2823 (2008).
- [S8] Nogués, J. & Schuller, I. K. Exchange bias. *J. Magn. Magn. Mater.* **192**, 203–232 (1999).
- [S9] Takahashi, M. & Tsunoda, M. Magnetic anisotropy of antiferromagnet and its role on the exchange bias in ferromagnetic/antiferromagnetic bilayers. *J. Phys. D: Appl. Phys.* **35**, 2365–2376 (2002).
- [S10] Scholl, A., Liberati, M., Arenholz, E., Ohldag, H. & Stöhr, J. Creation of an antiferromagnetic exchange spring. *Phys. Rev. Lett.* **92**, 247201 (2004).
- [S11] Martí, X. *et al.* Electrical measurement of antiferromagnetic moments in exchange-coupled IrMn/NiFe stacks. *Phys. Rev. Lett.* **108**, 017201 (2012).
- [S12] Stiles, M. D. & McMichael, R. D. Model for exchange bias in polycrystalline ferromagnet-antiferromagnet bilayers. *Phys. Rev. B* **59**, 3722–3733 (1999).

- [S13] Weber, M. C., Nembach, H., Hillebrands, B. & Fassbender, J. Modified Gilbert damping due to exchange bias in NiFe/FeMn bilayers. *J. Appl. Phys.* **97**, 10A701 (2005).
- [S14] Abdulahad, F. B., Hung, D.-S., Chiu, Y.-C. & Lee, S.-F. Exchange bias effect on the relaxation behavior of the IrMn/NiFe bilayer system. *IEEE Trans. Magn.* **47**, 4227–4230 (2011).
- [S15] Schellekens, A. J. *et al.* Determining the Gilbert damping in perpendicularly magnetized Pt/Co/AlO_x films. *Appl. Phys. Lett.* **102**, 082405 (2013).